

# Metadata of the article that will be visualized in OnlineFirst

ArticleTitle	3D Finite Element Analysis of Rock Deformation in Twin Circular Tunnels with a Transverse Gallery Using Plasticity and Time-Dependent Models	
Article Sub-Title		
Article CopyRight	The Author(s), under exclusive licence to Springer Nature Switzerland AG (This will be the copyright line in the final PDF)	
Journal Name	Geotechnical and Geological Engineering	
Corresponding Author	FamilyName	<b>Motta Quevedo</b>
	Particle	da
	Given Name	<b>Felipe Pinto</b>
	Suffix	
	Division	
	Organization	Federal University of Rio Grande do Sul/PPGEC
	Address	Osvaldo Aranha, Porto Alegre, RS, Zip-Code: 90.035-190, Brazil
	Phone	
	Fax	
	Email	motta.quevedo@ufrgs.br
	URL	
	ORCID	<a href="http://orcid.org/0000-0003-4171-1696">http://orcid.org/0000-0003-4171-1696</a>
Author	FamilyName	<b>Colombo</b>
	Particle	
	Given Name	<b>Carlos Alberto Magnus Maciel</b>
	Suffix	
	Division	
	Organization	Federal University of Rio Grande do Sul/PPGEC
	Address	Osvaldo Aranha, Porto Alegre, RS, Zip-Code: 90.035-190, Brazil
	Phone	
	Fax	
	Email	ca-colombo@hotmail.com
	URL	
	ORCID	<a href="http://orcid.org/0009-0008-2551-0548">http://orcid.org/0009-0008-2551-0548</a>
Author	FamilyName	<b>Bernaud</b>
	Particle	
	Given Name	<b>Denise</b>
	Suffix	
	Division	
	Organization	Federal University of Rio Grande do Sul/PPGEC
	Address	Osvaldo Aranha, Porto Alegre, RS, Zip-Code: 90.035-190, Brazil
	Phone	
	Fax	
	Email	denise.bernaud@ufrgs.br
	URL	
	ORCID	<a href="http://orcid.org/0000-0001-6365-3269">http://orcid.org/0000-0001-6365-3269</a>
Author	FamilyName	<b>Maghous</b>
	Particle	
	Given Name	<b>Samir</b>
	Suffix	
	Division	
	Organization	Federal University of Rio Grande do Sul/PPGEC
	Address	Osvaldo Aranha, Porto Alegre, RS, Zip-Code: 90.035-190, Brazil
	Phone	
	Fax	
	Email	samir.maghous@ufrgs.br
	URL	
	ORCID	<a href="http://orcid.org/0000-0002-1123-3411">http://orcid.org/0000-0002-1123-3411</a>

Schedule	Received Revised Accepted	30 Sep 2024  8 Mar 2025
Abstract	Resorting to a three-dimensional finite element framework, the paper investigates the instantaneous and long-term deformation in twin tunnels with connecting transverse gallery. Particular emphasis is dedicated to the assessment of combined effects induced by the time-dependent behavior of the constituent materials, twin tunnels proximity and tunnel junctions on the convergence profile. At the material level, the rock mechanical behavior is formulated within the context of coupled plasticity–viscoplasticity, which proves relevant for modeling the tunnel deformation in deep clayey rocks. As regards the time-dependent properties of the lining concrete, creep deformation is addressed by means of an aging viscoelastic model relying on the Bažant and Prasannan Solidification Theory, whereas the shrinkage deformation component is based on the formulation proposed in CEB-FIP MC90 standard. At the structure level, the deactivation-activation technique is employed in the three-dimensional finite element model to simulate the excavation/advancing face and lining installation processes. The accuracy of the approach is assessed by comparison of the model predictions with available analytical and numerical stress solutions derived in the context of simplified twin tunnel configurations. The three-dimensional computational model is then applied to analyze the deformation mechanisms in circular twin tunnels with a transverse gallery. The numerical simulations emphasized the significant deformation anisotropy induced by tunnels proximity, the peak convergence values observed at tunnel-gallery junction as well as the crucial role of time-dependent properties of concrete lining in controlling the tunnel deformation.	
Keywords (separated by '-' )	Twin tunnels - Transverse gallery - Plasticity-viscoplasticity coupling - Viscoelastic lining - Finite element model	

Footnote Information



## 2 **3D Finite Element Analysis of Rock Deformation in Twin 3 Circular Tunnels with a Transverse Gallery Using Plasticity 4 and Time-Dependent Models**

5 **Felipe Pinto da Motta Quevedo** · **Carlos Alberto Magnus Maciel Colombo** · **Denise Bernaud** ·  
6 **Samir Maghous**

7 Received: 30 September 2024 / Accepted: 8 March 2025  
8 © The Author(s), under exclusive licence to Springer Nature Switzerland AG 2025

9 **Abstract** Resorting to a three-dimensional finite  
10 element framework, the paper investigates the instan-  
11 taneous and long-term deformation in twin tunnels  
12 with connecting transverse gallery. Particular empha-  
13 sis is dedicated to the assessment of combined effects  
14 induced by the time-dependent behavior of the con-  
15 stituent materials, twin tunnels proximity and tunnel  
AQ1 junctions on the convergence profile. At the material  
17 level, the rock mechanical behavior is formulated  
18 within the context of coupled plasticity-viscoplas-  
19 ticity, which proves relevant for modeling the tun-  
20 nel deformation in deep clayey rocks. As regards  
21 the time-dependent properties of the lining concrete,  
22 creep deformation is addressed by means of an aging  
23 viscoelastic model relying on the Bažant and Prasan-  
24 nan Solidification Theory, whereas the shrinkage  
25 deformation component is based on the formulation  
26 proposed in CEB-FIP MC90 standard. At the struc-  
27 ture level, the deactivation-activation technique is

employed in the three-dimensional finite element  
28 model to simulate the excavation/advancing face and  
29 lining installation processes. The accuracy of the  
30 approach is assessed by comparison of the model pre-  
31 dictions with available analytical and numerical stress  
32 solutions derived in the context of simplified twin  
33 tunnel configurations. The three-dimensional com-  
34 putational model is then applied to analyze the defor-  
35 mation mechanisms in circular twin tunnels with a  
36 transverse gallery. The numerical simulations empha-  
37 sized the significant deformation anisotropy induced  
38 by tunnels proximity, the peak convergence values  
39 observed at tunnel-gallery junction as well as the cru-  
40 cial role of time-dependent properties of concrete lin-  
41 ing in controlling the tunnel deformation.  
42

**Keywords** Twin tunnels · Transverse gallery ·  
43 Plasticity-viscoplasticity coupling · Viscoelastic  
44 lining · Finite element model  
45

### 1 Introduction

The increasing development of tunnel infrastructures  
47 for transportation systems and facilities networks  
48 in urban, hilly or underwater environments requires  
49 rational and efficient use of underground space, lead-  
50 ing in many situations to tunneling nearby existing  
51 or new tunnels. The number of deep or shallow twin  
52 tunnels excavated in close proximity to each other  
53 has notably increased in the last years mainly due to  
54

A1 F. P. da Motta Quevedo · C. A. M. M. Colombo ·  
A2 D. Bernaud · S. Maghous  
A3 Federal University of Rio Grande do Sul/PPGEC, Osvaldo  
A4 Aranha, Porto Alegre, RS Zip-Code: 90.035-190, Brazil  
A5 e-mail: motta.quevedo@ufrgs.br  
A6 C. A. M. M. Colombo  
A7 e-mail: ca-colombo@hotmail.com  
A8 D. Bernaud  
A9 e-mail: denise.bernaud@ufrgs.br  
A10 S. Maghous  
A11 e-mail: samir.maghous@ufrgs.br

55 prevailing underground and geotechnical conditions  
 56 in congested urban areas. Resorting to the solution  
 57 of twin tunnels, each branch being devised for a flow  
 58 direction, also presents technical and safety advan-  
 59 tages such as the reduction of tunnel diameter. Fur-  
 60 thermore, in most cases of adjacent twin tunnels, the  
 61 construction of connecting transverse galleries is a  
 62 standard tunnel engineering practice either for safety  
 63 (emergency exit/access) or functionality (main-  
 64 tenance, service cross-passage) purposes.

65 The sequence of construction phases of parallel  
 66 twin tunnels running side-by-side as well as of the  
 67 transverse gallery is generally dictated by the engi-  
 68 neering practice and construction program. The tun-  
 69 nel junctions are usually constructed far behind the  
 70 advancing face of main tunnel to ensure the excava-  
 71 tion of latter slightly affects that of the junction gal-  
 72 lery (Chortis and Kavaadas 2021a; Insam et al. 2019).

73 In this context, understanding and assessing the  
 74 multiple interactions between the components of such  
 75 a tunnel material system, namely the closely-spaced  
 76 twin tunnels, the intersecting transverse gallery, the  
 77 support lining and the ground, is a fundamental and  
 78 challenging engineering issue that should be han-  
 79 dled during the planning stages for optimal design  
 80 and safety of the whole tunneling operations. Evi-  
 81 dence of interaction phenomena in twin tunnels and  
 82 tunnel junctions have been reported by many case  
 83 studies (e.g., Pöttler 1992; Nyren 1998; Hsiao et al.  
 84 2005; Sjöberg et al. 2006; Karakus et al. 2007; Afif-  
 85 ipour et al. 2011; Fortsakis et al. 2012; Farnoli et al.  
 86 2015; Li et al. 2016; Elwood and Martin 2016; Con-  
 87 nor Langford et al. 2016; Wan et al. 2017; Insam et al.  
 88 2019). From a structural design viewpoint, the analy-  
 89 sis of the complex interaction in such a tunnel system  
 90 is not an easy task since it inherently involves several  
 91 factors related to geometry and constitutive charac-  
 92 teristics as well as to the prevailing initial mechani-  
 93 cal state and the sequence of tunneling. In particular,  
 94 the computational evaluation of rock deformation and  
 95 lining loading near the region of tunnel-gallery inter-  
 96 section requires a three-dimensional modeling (e.g.,  
 97 Spyridis and Bergmeister 2015; Chortis and Kavaa-  
 98 das 2021b). The construction process of the trans-  
 99 verse gallery induces a stress redistribution within  
 100 the surrounding rock mass, which in turn results in  
 101 additional loading applied to the lining support of  
 102 the main tunnel. Furthermore, a key aspect of the  
 103 3D modeling is the ability to capture the interaction

104 effects on both short-term and long-term structural  
 105 behavior, which are mainly controlled by the time-  
 106 dependent rheological behavior of the rock and lining  
 107 material constituents. AQ?

108 As far as the computational tunnel interaction  
 109 modeling is concerned, most investigations addressed  
 110 the configuration of shallow adjacent or twin tunnels  
 111 (see for instance Karakus et al. 2007; Zheng et al.  
 112 2015; Do et al. 2014, 2016, 2022; Vlachopoulos et al.  
 113 2018; Forsat et al. 2022; Pedro et al. 2022; Phutthana-  
 114 non et al. 2023, to cite a few recent works), with par-  
 115 ticular focus on subsurface and surface interaction  
 116 effects, including evaluation of induced ground settle-  
 117 ment. In that respect, a comprehensive review of ref-  
 118 erence works on related topics may be found in Islam  
 119 and Iskander (2021).

120 Referring to the particular configuration of deep-  
 121 buried tunnels addressed in this paper, the following  
 122 analytical and numerical contributions to twin tun-  
 123 nels interaction modeling should be quoted. Analyti-  
 124 cal solutions for the stress distribution around unlined  
 125 and lined deep circular twin tunnels have been respec-  
 126 tively formulated in Guo et al. (2021a,  
 127 b) and Chen et al. (2019) within the framework of  
 128 plane strain assumption considering an elastic behav-  
 129 ior for the rock material. It has been found that the  
 130 interaction between the twin tunnels vanishes when  
 131 the tunnel spacing exceeds typically two to three tun-  
 132 nel diameters. Similar problem has been studied in  
 133 Ma et al. (2020) who considered unlined deep twin  
 134 circular tunnels excavated in a homogeneous elasto-  
 135 plastic medium. The approximate analytical solution  
 136 formulated for the stresses and the plastic zone extent  
 137 has been verified through comparison with numerical  
 138 results using FLAC3D software. The authors carried  
 139 out a parametric study to assess the influence of twin  
 140 tunnels spacing, rock strength properties and in-situ  
 141 initial stresses on the shape and extent of the plastic  
 142 zones.

143 Several 3D numerical analyses have investigated  
 144 the mechanical interaction in deep adjacent tunnels  
 145 (see for instance Chen et al. 2009; Fortsakis et al.  
 146 2012; Vlachopoulos and Diederichs 2014; Shaofeng  
 147 et al. 2018; Chortis and Kavvadas 2021a, among oth-  
 148 ers). One may refer to Chortis and Kavvadas (2021a)  
 149 for a more exhaustive review on 3D computational  
 150 approaches dealing with such a problem. Overall,  
 151 most of these studies emphasized the crucial effect  
 152 of pillar width on interaction phenomena occurring

153 in the area between adjacent tunnels. The numerical simulations also indicated that the redistribution  
154 of strains and stresses induced in the zone between  
155 adjacent tunnels by the construction process may be  
156 fundamental to devise adequate support/lining system  
157 (Fortsakis et al. 2012; Chortis and Kavvadas 2021a).  
158 In this context, Chortis and Kavvadas (2021a) carried  
159 out parametric 3D finite element analyses to assess  
160 the interaction between deep parallel twin tunnels,  
161 with circular and non-circular cross-section, exca-  
162 vated in an elastoplastic rock mass and supported by  
163 a linear elastic shotcrete lining. The study focused the  
164 interaction analysis on the axial forces that develop in  
165 the primary lining of the twin tunnels by considering  
166 the effects of geometrical, geotechnical and material  
167 constitutive parameters as well as of the construc-  
168 tion conditions. In addition, an important conclusion  
169 drawn from these studies is that 2D analyses cannot  
170 realistically capture the purely 3D interaction nature  
171 of the tunneling problem (Vlachopoulos and Dieder-  
172 ichs 2014).

173 However, few numerical works addressed the  
174 interaction phenomena associated with the excava-  
175 tion of transverse gallery connecting the main tun-  
176 nels. This is mainly due to the fact the numerical  
177 simulation of the tunnel junction area would rely on  
178 complex 3D geometry discretization together with a  
179 large number of calculation steps to provide realis-  
180 tic modeling of the sequentially tunneling process,  
181 thus leading to time-consuming procedures. Recent  
182 representative works include references (Hsiao  
183 et al. 2009; Spyridis and Bergmeister 2015; Li et al.  
184 2016; Liu et al. 2017; Chortis and Kavvadas 2021b,  
185 2023a, 2023b). As reported in Chortis and Kavva-  
186 das (2021b), the interaction between the transverse  
187 gallery and the main longitudinal tunnels signifi-  
188 cantly modifies the deformation and stress states  
189 of the primary support and the surrounding rock  
190 mass at the intersection area, making 3D numeri-  
191 cal simulations necessary for the realistic design of  
192 such complex structure. It is pointed out that most  
193 of the numerical studies were limited to case studies  
194 and, as such, cannot be provide design guidelines  
195 for more general tunnel junctions. In that respect,  
196 one should particularly quote the contributions by  
197 Chortis and Kavvadas (2021b, 2023a, 2023b) who  
198 investigated the mechanical interaction in deep tun-  
199 nel junction by means of 3D finite element analy-  
200 ses. Based on a comprehensive set of parametric

201 3D finite element studies, these authors formulated  
202 design charts for the axial forces and bending  
203 moments acting on the primary support in the inter-  
204 section zone between the main and junction tunnels.

205 Existing literature addressing the mechan-  
206 ical interaction in deep twin tunnels with connect-  
207 ing transverse galleries has mainly focus on the  
208 response associated with instantaneous reversible-  
209 irreversible behavior of the rock mass and lining  
210 constituent materials. It is however well estab-  
211 lished that creep is an essential component of rock  
212 deformation in deep tunnels, leading to progres-  
213 sive development of tunnel convergence and lining  
214 loading during the construction phase and extend-  
215 ing over months or even years. In this context, the  
216 purpose of the present study is to investigate the  
217 implications of time-dependent constitutive proper-  
218 ties of rock and support shotcrete/concrete materials  
219 on the short-term and long-term structural behavior.  
220 The main novelty of the proposed approach is two-  
221 fold: (i) Formulation of proper constitutive behavior  
222 for the rock in the framework of coupled plasticity-  
223 viscoplasticity as well as for the lining concrete in  
224 the context of aging viscoelasticity, and (ii) Com-  
225 putational incorporation of the previous constitu-  
226 tive models into a finite element code devised for  
227 dealing with three-dimensional simulation of defor-  
228 mation in complex tunnel systems. At the material  
229 level, the 3D computational model integrates the  
230 constitutive state equations formulated for the rock  
231 in the framework of coupled plasticity-viscoplastic-  
232 ity, which proves relevant for capturing both irre-  
233 versible instantaneous response (plasticity) as well  
234 as the delayed irreversible response (viscoplastic-  
235 ity). Creep behavior of the lining material, typically  
236 shotcrete, is described by means of an aging visco-  
237 elastic model that notably accounts for the proper-  
238 ties at early age. At the tunnel structure level, the  
239 constitutive modeling as well as the related numeri-  
240 cal integration schemes are developed and imple-  
241 mented within a specific UPF/USERMAT proce-  
242 dure of ANSYS standard software (ANSYS 2018),  
243 which shall be used for the tunnel simulations. The  
244 finite element modeling developed in this paper can  
245 be viewed as specifically devised tool for address-  
246 ing the three-dimensional interaction induced by the  
247 construction process of closely-spaced twin tunnels  
248 with transverse gallery junction. The last part of the  
249 paper provides several numerical simulations that  
250

251 illustrate the ability to deal with such a problem in  
252 highly complex setting and to provide preliminary  
253 insight into the involved interactions.

## 254 2 Fundamental Assumptions

255 The basic assumptions of the constitutive and compu-  
256 tational modeling, as well as related limitations, are  
257 summarized as follows:

- 258 • Only the configuration of deep tunnels shall  
259 be considered in the subsequent analysis, thus  
260 neglecting deformations caused by surface loads  
261 and settlements arising from the excavation pro-  
262 cess.
- 263 • Although material heterogeneity and behavior ani-  
264 sotropy are inherent features of soils and rocks,  
265 the rock mass is modeled throughout the paper as  
266 a homogeneous and isotropic continuous medium.  
267 At the scale adopted for tunnel modeling (mac-  
268 roscopic scale), this assumption means in par-  
269 ticular that the possible micro-heterogeneities,  
270 such isotropic distributions of joints or cracks  
271 present at the finer scale, are accounted for in the  
272 homogenized behavior by means of a preliminary  
273 homogenization process (e.g., Nemat-Nasser and  
274 Hori 1993; Deudé et al. 2002; de Buhan et al.  
275 2002; Marmier et al. 2007; Aguiar and Maghous  
276 2023). Clearly enough, the framework of contin-  
277 uum modeling adopted in the paper would reveal  
278 questionable when the rock mass is cut by a few  
279 macroscale fracture joints. Among the theoretical  
280 and numerical approaches dealing with stress and  
281 deformation distributions around tunnels exca-  
282 vated in jointed rock masses or fault rock zones,  
283 one may quote for instance the works of Maghous  
284 et al. (2008), Maghous et al. (2014a), Nikadat and  
285 Marji (2016) or Abdollahi et al. (2019).
- 286 • The rock mass is phenomenologically modeled  
287 using an elastoplastic-viscoplastic rheological law  
288 to capture instantaneous and long-term responses.  
289 This approach disregards the aspect connected  
290 temperature gradients, water flow and porome-  
291 mechanics coupling. Regarding the latter aspect, sev-  
292 eral works have addressed the modeling of rock  
293 deformation in the context of poroelasticity (e.g.,  
294 Maghous et al. 2013, 2014b; Abdollahipour et al.  
295 2016a, 2016b, to cite a few).

- Twin tunnels are often designed considering a time gap between excavation fronts. However, the finite element simulations assume synchronous excavation steps to ensure symmetry conditions. 296
- The simulation excavation processes are carried out assuming a constant tunnel advancement rate (i.e., constant excavation speed), together with a constant thickness of concrete lining. In addition, the concrete lining is viewed in the modeling as a three-dimensional continuum whose time-evolving properties are homogeneous along the thickness. In that respect, no distinction is made between initial and secondary support systems. 307
- Effects of temperature and humidity that may affect the viscoelastic behavior of lining concrete are disregarded. 311
- Perfect bonding is assumed at the interface between concrete lining and the rock mass. 312

## 3 Constitutive Model of the Rock Material

314 Time-dependent phenomena associated with the delayed behavior of the constitutive material are key aspects of deformation in tunnel structures excavated in deep clayey rocks (see for instance Rousset 1988; Nguyen Minh and Rousset 1987; Giraud and Rousset 1996, to cite a few). In most computational analyses developed for tunnel engineering design, this issue is generally addressed by means of viscoplastic constitutive behavior. While such constitutive models could relevantly model the transient and long-term deformation, they seem however inadequate to capture the influence of short-term events (tunnelling and support placement phases) on the final stability of the structure. In particular, an analysis of tunnel deformation based on a viscoplastic model would suggest that the ultimate support pressure at tunnel structure equilibrium mainly depends on the closure rate at the moment when the contact between lining and rock mass is achieved (e.g., Nguyen Minh and Rousset 1987), thus disregarding the irreversible effects rising in the initial construction phases. Indeed, during the primary stages of tunnel excavation, the surrounding rock mass is subjected to severe loading conditions and high strain rates, which may lead to yielding associated with high instantaneous irreversible strains near the tunnel wall, and can therefore affect the long-term equilibrium of the structure. It is

thus of fundamental concern to formulate a constitutive model that incorporates both instantaneous and delayed irreversible components of the rock material. For this purpose, the present analysis considers a constitutive model that includes both instantaneous plasticity to describe short-term material yielding and viscoplasticity to represent delayed behavior. The formulation of the coupled plasticity-viscoplasticity rheological model is based on that originally proposed in Nguyen Minh and Rousset (1987) and Rousset (1988). Previous studies have implemented this plastic-viscoplastic model for computational analysis of deformation in single tunnels (e.g., Bernaud and Rousset 1993; Piepi 1995; Giraud and Rousset 1996; Quevedo 2021). For the sake of brevity, only the main features of this constitutive model shall be summarized below. Detailed description of the model, including application and validation in the context of single tunnel structures may be found in Quevedo et al. (2022b). Finite element implementation of this model in the USERMAT procedure of ANSYS software is also described in Quevedo (2021).

The elastoplastic-viscoplastic model is formulated based on a serial association of the elastoplastic and viscoplastic constitutive models. The local strain rate  $\dot{\epsilon}$  is split into three contributions  $\dot{\epsilon} = \dot{\epsilon}^e + \dot{\epsilon}^p + \dot{\epsilon}^{vp}$ , so that the constitutive relationships relating the Cauchy stress rate  $\dot{\sigma}$  and strain rate components can be written as:

$$\dot{\sigma} = \mathbf{D} : \dot{\epsilon}^e = \mathbf{D} : (\dot{\epsilon} - \dot{\epsilon}^p - \dot{\epsilon}^{vp}) \quad (1)$$

In the above relationship,  $\dot{\epsilon}^e$ ,  $\dot{\epsilon}^p$  and  $\dot{\epsilon}^{vp}$  represent respectively the elastic, plastic and viscoplastic strain rate, and  $\mathbf{D}$  denote the fourth-order isotropic elastic linear constitutive tensor. Tensor  $\mathbf{D}$  is defined by the rock mass elastic Young modulus  $E$  and Poisson ratio  $v$ . The one-dimensional representation of the constitutive behavior is shown in Fig. 1.

In the three-dimensional context, the plasticity component of constitutive behavior is described by a Drucker-Prager plastic flow surface given by:

$$f(\sigma, q) = f(I_1, J_2, q) = \beta_1 I_1 + \beta_2 \sqrt{J_2} - q(\alpha) \quad (2)$$

In the above Eq. (2),  $I_1$  is the first invariant of the stress tensor,  $J_2$  the second invariant of the deviator tensor and  $\beta_1$ ,  $\beta_2$  and  $q(\alpha)$  are strength parameters related to the friction angle  $\phi$  and cohesion  $c(\alpha)$ , respectively. Drucker-Prager plasticity surface inscribed to the

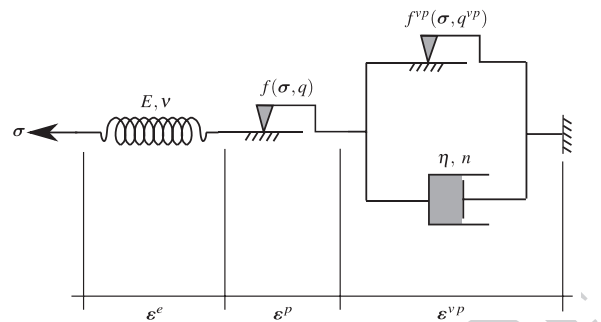


**Fig. 1** Rheological representation of the elastoplastic-viscoplastic model

Mohr-Coulomb surface shall be considered throughout the subsequent analysis (Bernaud 1991):

$$\beta_1 = \frac{(k-1)}{3}, \beta_2 = \frac{(2k+1)}{\sqrt{3}}, q(\alpha) = 2\sqrt{k}c(\alpha) \quad (3)$$

where  $k = (1 + \sin\phi)/(1 - \sin\phi)$ . The internal variable  $\alpha$  is the equivalent plastic strain  $\bar{\epsilon}^p$  used to simulate strain hardening/softening phenomena. However, for this study, we adopt perfect plasticity, meaning that the cohesion  $c$  is a constant parameter. Referring to Fig. 1, the viscoplastic strain component is defined by means of the threshold stress function  $f^{vp}$  and the dash-dot viscosity parameters. A similar expression to that introduced in Eq. (2) for the plastic yield surface will be adopted throughout the analysis for the viscoplasticity surface  $f^{vp}$ , with the viscoplastic cohesion and friction angle parameters ( $c^{vp}$ ,  $\phi^{vp}$ ) instead of ( $c$ ,  $\phi$ ). Accordingly, the viscoplastic counterparts of parameters  $\beta_1$  and  $\beta_2$  in (3) shall be computed using  $k^{vp} = (1 + \sin\phi^{vp})/(1 - \sin\phi^{vp})$ . Likewise, the viscoplastic strength parameter is defined by  $q^{vp} = 2\sqrt{k^{vp}}c^{vp}$  in which the cohesion  $c^{vp}$  is a constant parameter, i.e., perfect viscoplasticity. The plastic flow rule is given by:

$$\dot{\epsilon}^p = \begin{cases} \lambda \frac{\partial g}{\partial \sigma} & \text{for } f > 0 \\ 0, & \text{for } f \leq 0 \end{cases} \quad (4)$$

where  $\lambda$  is the plasticity multiplier and  $g$  is a potential flow function analogous to  $f$  used to simulate the volume dilatation during the evolution of plastic deformations. However, for this analysis, was used associated plasticity, i.e.,  $g = f$ . The plastic multiplier is obtained through the consistency condition

421  $\dot{f} = 0$ . Numerical details of this implementation can  
 422 be found in Quevedo et al. (2022b). For viscoplastic  
 423 flow rule we have,

$$424 \quad \dot{\epsilon}^{vp} = \lambda^{vp} \frac{\partial f^{vp}}{\partial \sigma} \quad (5)$$

425  
 426 In contrast to the plastic multiplier, the viscoplastic  
 427 multiplier  $\lambda^{vp}$  is independent of a consistency like  
 428 condition. As a result, its expression is explicit. Based  
 429 on the framework of generalized Perzyna's overstress  
 430 theory (Perzyna 1966), its expression may be derived  
 431 as follows:

$$432 \quad \lambda^{vp} = \frac{\Phi(\sigma, q^{vp})}{\eta} \quad \text{and} \quad \Phi = \frac{f^{vp}(\sigma, q^{vp})^n}{f_0} \quad (6)$$

433  
 434 where  $\Phi$  is the overstress function,  $\eta$  is the dynamic  
 435 viscosity constant,  $n$  is the dimensionless parameter  
 436 that gives the form of the power law,  $f_0$  a parameter  
 437 conveniently adopted and  $\langle * \rangle$  is the McCauley func-  
 438 tion which is 0 when  $* < 0$ , i.e. viscoplastic flow will  
 439 only occur when the overstress function is positive.

440 In this coupled model, when  $\phi = \phi^{vp}$ , cohesion  
 441 entirely controls the evolution of local mechanical  
 442 fields. Specifically, when  $c \rightarrow \infty$  and  $c^{vp} \rightarrow \infty$ , the  
 443 system achieves a purely elastic solution. The solution  
 444 becomes purely elastoviscoplastic with  $c \rightarrow \infty$ , while  
 445 a pure elastoplastic solution emerges with  $c^{vp} \rightarrow \infty$ .  
 446 In the coupled analysis, condition  $c^{vp} < c$  is adopted,  
 447 allowing the viscoplastic domain to occur without  
 448 plasticity. However, in the presence of plasticity, vis-  
 449 cosus effects become inevitable. Figure 2 illustrates  
 450 these domains in principal stress space.

#### 451 4 Constitutive Model of the Lining

452 Shrinkage and creep phenomena represent fun-  
 453 fundamental components of concrete deformation  
 454 processes that are expected to naturally affect the  
 455 instantaneous as well as the transient and long-  
 456 term behavior of structures involving such mate-  
 457 rial. However, most of the tunnel design analyses  
 458 consider the concrete involved in lining systems  
 459 as a linear elastic material. From a phenomeno-  
 460 logical point of view, creep of concrete refers to the  
 461 time-dependent deformation induced by sustained  
 462 loading, whereas shrinkage deformation refers  
 463 to the volume decrease caused by drying. As far

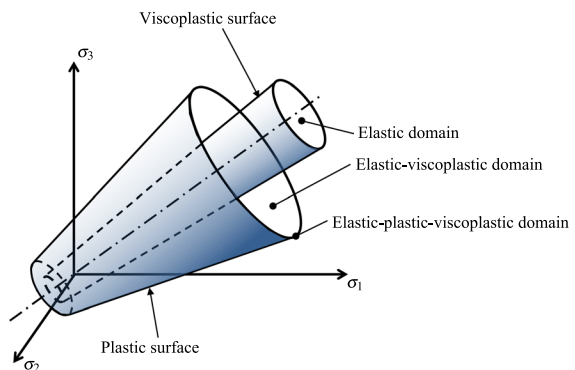


Fig. 2 Elastoplastic-viscoplastic domains

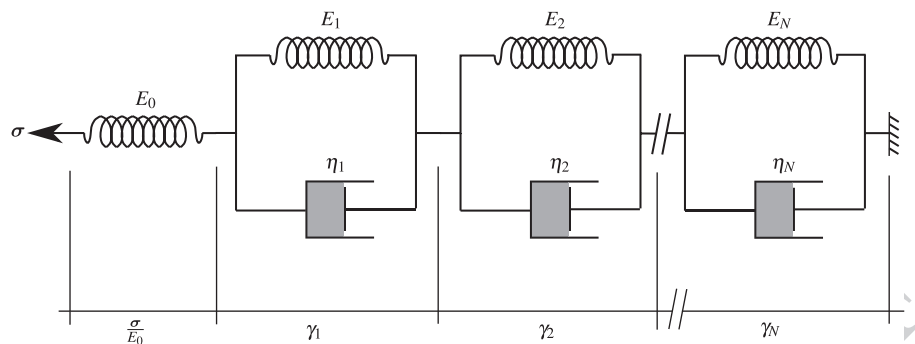
464 as deformation in tunnel structures is concerned,  
 465 creep and shrinkage have an important effect on  
 466 the performance of the concrete lining and conse-  
 467 quently on its contribution to controlling the long-  
 468 term convergence of the tunnel. To account for such  
 469 constitutive features, the concrete creep deforma-  
 470 tion is addressed by means of an aging viscoelastic  
 471 rheological model relying on Solidification Theory  
 472 (Bažant and Prasannan 1989a, 1989b). The visco-  
 473 elastic model is described by a Generalized Kelvin-  
 474 chain as depicted in Fig. 3. The mechanical param-  
 475 eters that define such a rheological model are the  
 476 springs stiffness and dash-pots viscosity. The model  
 477 parameters are calibrated based on the CEB-FIP  
 478 MC90 standard specifications formulation reported  
 479 in CEB-FIP (1993). One may refer to Quevedo et al.  
 480 (2018), Quevedo et al. (2022a) for detailed descrip-  
 481 tion of the calibration procedure. As regards the  
 482 concrete deformation associated with shrinkage, the  
 483 isotropic formulation proposed in CEB-FIP MC90  
 484 standard (CEB-FIP 1993) is adopted in the present  
 485 modeling and subsequent computational analyses.  
 486 Full details regarding model definition and related  
 487 finite element implementation may be found in  
 488 Quevedo (2017) and Quevedo et al. (2022a).

489 Accordingly, the constitutive equations for con-  
 490 crete lining relating the stress and strain rate can be  
 491 expressed in the framework of infinitesimal strain  
 492 analysis as:

$$\dot{\sigma} = \mathbf{D} : \dot{\epsilon}^e = \mathbf{D} : \dot{\epsilon} - \mathbf{D} : \dot{\epsilon}^{sh} - \mathbf{D}^* : \dot{\epsilon}^{cr} \quad (7)$$

493  
 494 In the above relationship (7),  $\dot{\epsilon}^{sh}$  and  $\dot{\epsilon}^{cr}$  are  
 495 respectively the shrinkage and creep strain rates.  
 496

**Fig. 3** Generalized Kelvin model for uniaxial concrete viscoelasticity



497 The fourth-order tensors  $\mathbf{D}$  and  $\mathbf{D}^*$  refer to the iso-  
 498 tropic elastic linear constitutive tensor and modified  
 499 constitutive tensor that incorporate the aging vis-  
 500 coelastic properties of the concrete, respectively.

501 For the numerical implementation purposes,  
 502 relationship (7) may conveniently be written in  
 503 incremental form:

$$504 \quad \Delta\sigma = \mathbf{D} : \Delta\epsilon - \mathbf{D} : \Delta\epsilon^{sh} - \mathbf{D}^* : \Delta\epsilon^{cr} \quad (8)$$

505 As mentioned above, isotropic formulation is  
 506 considered for shrinkage, so that increment of  
 508 shrinkage strain in (8) reads:

$$509 \quad \Delta\epsilon^{sh} = \Delta\epsilon_{sh}(t_s) \quad (9)$$

510 where  $t_s$  represents the concrete curing time, and  $\Delta\epsilon_{sh}$   
 511 is the variation in magnitude of the concrete deforma-  
 512 tion associated with shrinkage (the dependency  $\Delta\epsilon_{sh}$   
 513 of on current time is omitted). The latter expression is  
 515 determined based on CEB-FIP MC90 standard speci-  
 516 fications (CEB-FIP 1993).

517 Regarding the increment of creep strain  $\Delta\epsilon^{cr}$   
 518 introduced in Eq. (8), its value is computed mak-  
 519 ing use of the incremental algorithm developed by  
 520 Bažant and Prasannan (1989a, 1989b), together  
 521 with a model calibration that incorporates CEB-FIP  
 522 MC90 standard formulation (CEB-FIP 1993). More  
 523 precisely, the three-dimensional ageing viscoelas-  
 524 tic behavior of isotropic concrete is defined by the  
 525 Generalized Kelvin model shown in Fig. 3 that is  
 526 adopted for the relaxation modulus under uniaxial  
 527 stress, whereas the Poisson ratio is assumed to be  
 528 time independent within the time interval of anal-  
 529 ysis. Referring to the notations of Fig. 3, the pro-  
 530 cedure for the identification of model parameters  
 531 is achieved by comparing the creep functions pro-  
 532 vided in references Bažant and Prasannan (1989a,

1989b) and CEB-FIP (1993), leading to the follow-  
 533 ing equivalence:

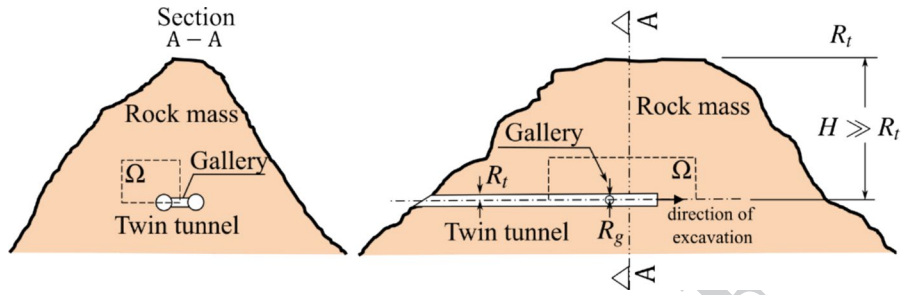
$$534 \quad E_0 = E_c(t_0), \gamma(t - t_0) \\ 535 \quad = \beta_c(t - t_0), \frac{1}{v(t)} = \frac{\phi_0(t_0)}{E_{ci}} \text{ and } \frac{1}{\eta(t)} \rightarrow 0 \quad (10)$$

536 in which  $t$  refers to the current time value and  $t_0$  to the  
 537 concrete age at the instant of load application (time  
 538 interval  $t - t_0$  is generally referred to as loading time  
 539 or loading age). In the Generalized Kelvin model  
 540 introduced by Bažant and Prasannan (1989a, 1989b),  
 541  $E_0$  is the instantaneous elasticity modulus of the con-  
 542 crete formed aggregates and cement paste particles,  
 543  $\gamma(t - t_0) = \sum_{i=1}^N \gamma_i$  is the microviscoelastic deforma-  
 544 tion of the volume fraction  $v(t)$  of solidified concrete  
 545 and  $\eta(t)$  is the apparent macroscopic viscosity. In the  
 546 CEB-FIP MC90 formulation (CEB-FIP 1993),  $E_c(t_0)$   
 547 stands for the tangent elastic modulus of concrete at  
 548 the instant of the loading application  $t_0$ ,  $\beta_c(t - t_0)$  is  
 549 a coefficient that depends on the loading age  $t - t_0$ ,  
 550  $\phi_0(t_0)$  is a coefficient defining the delayed strain  
 551 when loaded at age  $t_0$  of the concrete, and  $E_{ci}$  repre-  
 552 sents the tangent elasticity modulus of the concrete at  
 553 the age of 28 day.

## 5 Spatial and Time Discretization of the Domain

The geometry model of analyzed domain  $\Omega$  is sche-  
 556 matically displayed in Fig. 4. It consists of a system  
 557 of deep twin tunnels connected with a transverse gal-  
 558 lery. The radius of the circular longitudinal tunnels is  
 559 denoted by  $R_t$ , whereas that of the circular connect-  
 560 ing gallery is denoted by  $R_g \leq R_t$ . The underground  
 561

**Fig. 4** Schematic representation of the twin tunnels geometry problem



562 structure is excavated in a homogeneous rock mass at  
563 great depth  $H \gg R_t$ .

564 Within the analyzed material domain, the initial  
565 stress state prevailing in the rock mass prior to the  
566 tunnel excavation process is defined by constant ver-  
567 tical and horizontal geostatic stress  $\sigma_v$  and  $\sigma_h$ , taking  
568 the following form:

$$569 \quad \sigma_0 = -\sigma_v \mathbf{e}_y \otimes \mathbf{e}_y - \sigma_h (1 - \mathbf{e}_y \otimes \mathbf{e}_y) \quad (11)$$

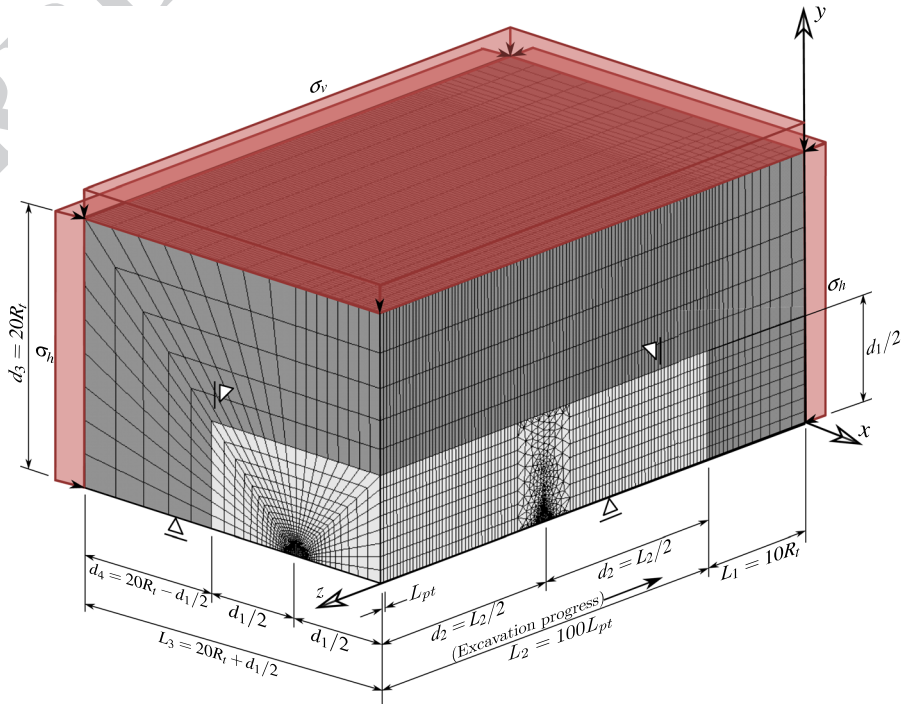
570

571 where  $\mathbf{e}_y$  is the upward unit vector parallel to verti-  
572 cal direction. The initial horizontal stress is generally  
573 related to the vertical stress by means of the hori-  
574 zontal thrust coefficient  $\sigma_h = k_0 \sigma_v$ . Starting from the  
575 initial configuration of the material system  $\Omega$ , the

processes of excavation (advancing face) and lining  
576 placement are simulated by means of the “activation/  
577 deactivation” technique (Bernaud et al. 1995, 2009;  
578 Maghous et al. 2012; Quevedo et al. 2022a).  
579

580 The geometry material domain  $\Omega$  considered for  
581 the finite element simulations, including tunnelling  
582 and deformation analysis, is defined by a parallel-  
583 epiped volume of dimensions  $(L_1 + L_2) \times L_3 \times d_3$   
584 (Fig. 5). Owing to the symmetry of the problem,  
585 only the material domain  $\{x \leq 0, y \geq 0\}$  is consid-  
586 ered for F.E discretization and analysis. Referring to  
587 the notations of Fig. 5,  $d_1$  is the distance between the  
588 axes of longitudinal tunnels,  $L_2$  represents the total  
589 length along longitudinal direction  $\mathbf{e}_z$  of the cylin-  
590 drical volume to be excavated that is considered in

**Fig. 5** Mesh, dimensions and boundary conditions of the 3D twin tunnel domain



591 the numerical simulation,  $d_3$  is the thickness along  
 592 vertical direction  $\mathbf{e}_y$  of material domain  $\Omega$ ,  $L_1$  stands  
 593 for the length of unexcavated region after total exca-  
 594 vation process,  $L_3$  is the total length along transver-  
 595 sal direction  $\mathbf{e}_x$  of discretized material domain,  $d_2$   
 596 characterizes the location of the circular transverse  
 597 axis gallery that intersects the longitudinal tunnel  
 598 at  $z = L_1 + d_2$ . The length of the excavation step  
 599 adopted will be denoted by  $L_{pr}$ .

600 Referring to the geometry model sketched in  
 601 Fig. 5, the boundary conditions read as follows:

602 • Planes of symmetry

$$603 \quad \mathbf{u} \cdot \mathbf{e}_x = 0 \quad ; \quad \boldsymbol{\sigma} \cdot \mathbf{e}_y = \boldsymbol{\sigma} \cdot \mathbf{e}_z = 0 \quad \text{at} \quad x = 0 \quad (12)$$

$$605 \quad \mathbf{u} \cdot \mathbf{e}_y = 0 \quad ; \quad \boldsymbol{\sigma} \cdot \mathbf{e}_x = \boldsymbol{\sigma} \cdot \mathbf{e}_z = 0 \quad \text{at} \quad y = 0 \quad (13)$$

607 • Left-lateral plane

$$608 \quad \boldsymbol{\sigma} \cdot \mathbf{e}_x = -\sigma_h \mathbf{e}_x \text{ at } x = -L_3 \quad (14)$$

610 • Upper plane

$$611 \quad \boldsymbol{\sigma} \cdot \mathbf{e}_y = -\sigma_v \mathbf{e}_y \text{ at } x = d_3 \quad (15)$$

613 • Front and back planes

$$614 \quad \boldsymbol{\sigma} \cdot \mathbf{e}_z = -\sigma_h \mathbf{e}_z \text{ at } z = 0 \quad (16)$$

$$616 \quad \mathbf{u} \cdot \mathbf{e}_z = 0 \quad ; \quad \boldsymbol{\sigma} \cdot \mathbf{e}_x = \boldsymbol{\sigma} \cdot \mathbf{e}_y = 0 \quad \text{at} \quad z = L_1 + L_2 \quad (17)$$

618 In the above expressions, vector  $\mathbf{u}$  refers to the dis-  
 619 placement field. The finite element model including  
 620 geometrical discretization and boundary conditions is  
 621 illustrated in Fig. 5. The mesh used in the simulations  
 622 consists of 119740, 182470 or 221104 total elements  
 623 (hexahedra and tetrahedra), depending on the value  
 624 of spacing between longitudinal tunnels. To increase  
 625 the accuracy of the model predictions in the inter-  
 626 section zone, the region surrounding the transverse  
 627 gallery (including part of the longitudinal tunnel) is  
 628 discretized by means 10-node quadratic tetrahedral  
 629 elements, whereas 8-node trilinear hexahedral ele-  
 630 ments are used for the remaining part of the structure.  
 631 Furthermore, a refined meshing is used for discretiz-  
 632 ing the zones surrounding the longitudinal and trans-  
 633 verse gallery. These zones whose mechanical state is

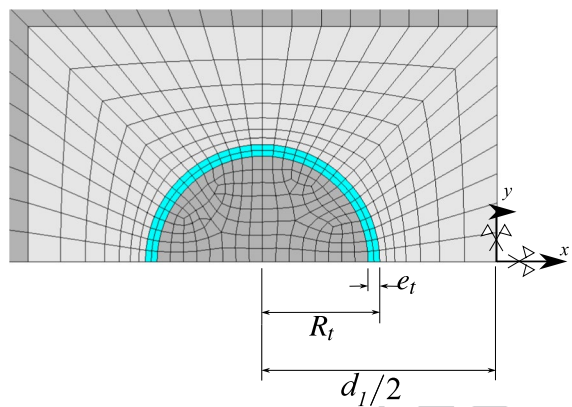


Fig. 6 Detail 1—Mesh in longitudinal tunnel cross-section with spacing  $d_1 = 4R_t$

significantly affected by the tunnelling process are  
 634  
 635 indicated by light gray color in Fig. 5.

Regarding the F.E discretization of the geometry  
 636 domain, it is observed that a mesh sensitivity study  
 637 was previously conducted to ensure the mesh conver-  
 638 gence. The latter study notably included a compari-  
 639 son of the numerical results with available solutions  
 640 (such as those provided in Sect. 6). The mesh density  
 641 was thus defined based on a balance between accu-  
 642 racy and computational cost efficiency. Figures 6, 7,  
 643 8, 9 and 10 display some details regarding the geom-  
 644 etry and F.E discretization of the structure. Figure 6  
 645 presents some details of the longitudinal tunnel cross-  
 646 section in a  $xy$  plane, together with the layer of con-  
 647 crete lining (in sky blue color), parameter  $e_t$  being the  
 648 thickness of the lining. Installation of the lining (shot-  
 649crete or precast concrete) is simulated in the F.E mod-  
 650 eling by progressive activation of the corresponding  
 651 elements, which consists in assigning to these ele-  
 652 ments the concrete mechanical properties.

An important issue investigated in this work is  
 654 the influence of the spacing  $d_1$  between twin tun-  
 655 nels on their convergence. Figures 7 and 8 illustrate  
 656 the spatial discretization of the gallery region as well  
 657 as of the connection with the longitudinal tunnel.  
 658 Three values shall be considered for the spacing  $d_1$   
 659 in the numerical simulations, namely  $d_1 = 16R_t$ ,  $8R_t$ ,  
 660 and  $4R_t$ . The layer of concrete lining of thickness  $e_g$   
 661 installed along the gallery wall is indicated by red  
 662 color in the figures. Without introducing additional  
 663 modeling restriction and for the sake of simplicity,  
 664 the value of the gallery radius is fixed to  $R_g = 2/3R_t$ .  
 665 The same lining system (same concrete material and

**Fig. 7** Geometry and F.E mesh of gallery cross-section for configurations  $d_1 = 16R_t$ ,  $d_1 = 8R_t$  and  $d_1 = 4R_t$

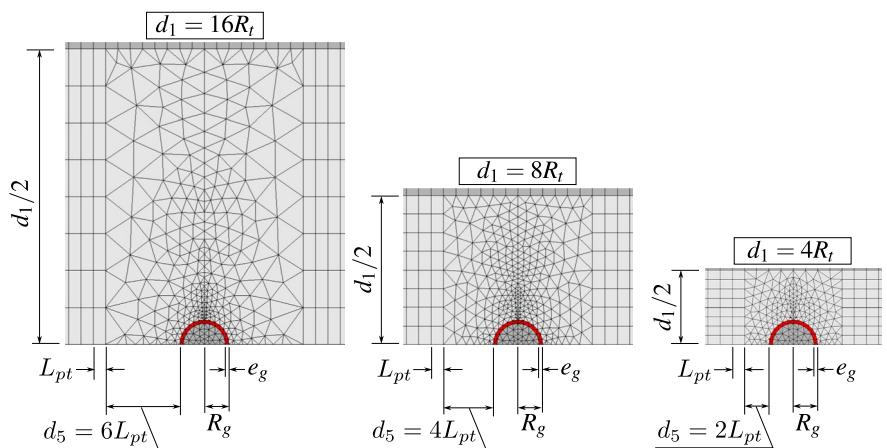
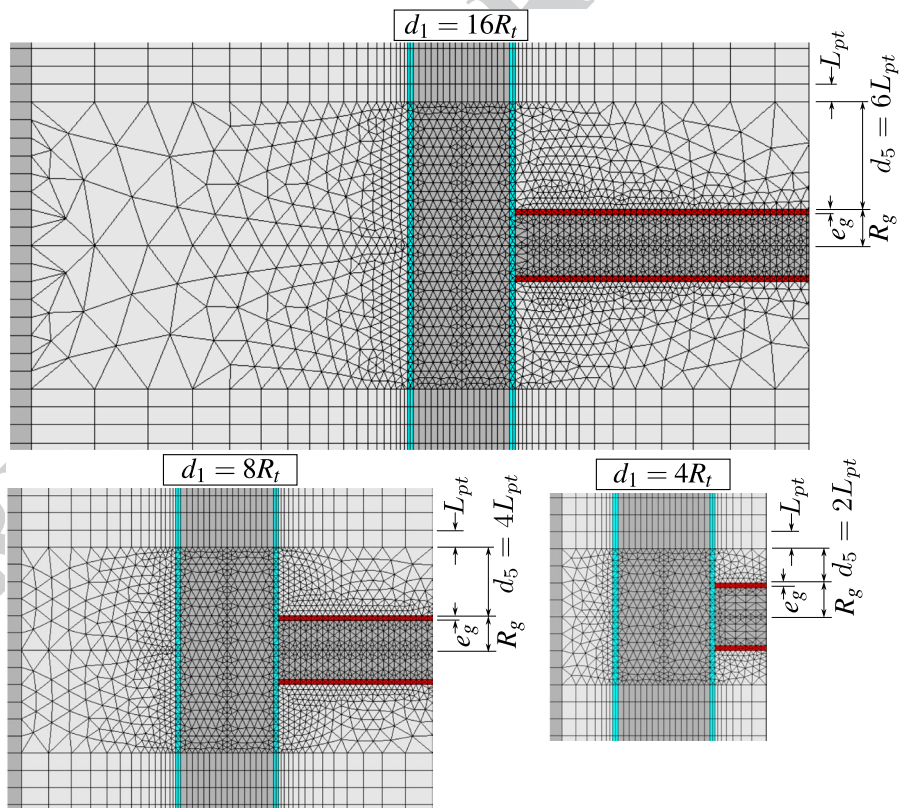


**Fig. 8** Views of longitudinal tunnel and gallery in the symmetry plane  $y = 0$  for configurations  $d_1 = 16R_t$ ,  $d_1 = 8R_t$  and  $d_1 = 4R_t$



667 layer thickness) is considered for both longitudinal  
668 tunnels and gallery. As regards the discretization of  
669 the region surrounding the gallery, parameters  $d_5$  and  
670  $d_1$  define the size in a  $yz$  plane of the transition region  
671 involving the tetrahedral finite elements. Figure 9 pro-  
672 vides a view of the transition region and tunnel/gal-  
673 lery intersection zone.

Finally, Fig. 10 presents the F.E mesh used for  
674 the layer of concrete lining in both the longitu-  
675 dinal layer (in sky blue color) and the gallery (in  
676 red color) for the three configurations  $d_1 = 16R_t$ ,  
677  $d_1 = 8R_t$  and  $d_1 = 4R_t$ , with specific details on the  
678 junction region of the gallery and the longitudinal  
679 tunnel. For the illustration purposes, symmetry with  
680 respect to plane  $y = 0$  has been used to complete  
681

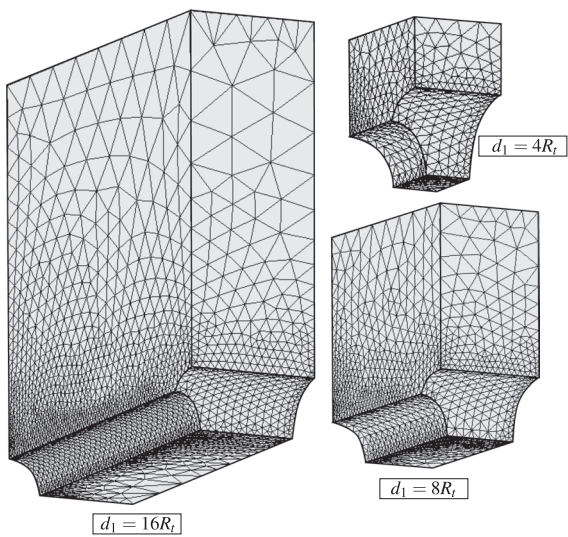


**Fig. 9** View of the transition and tunnel/gallery intersection zones for configurations  $d_1 = 16R_t$ ,  $d_1 = 8R_t$  and  $d_1 = 4R_t$

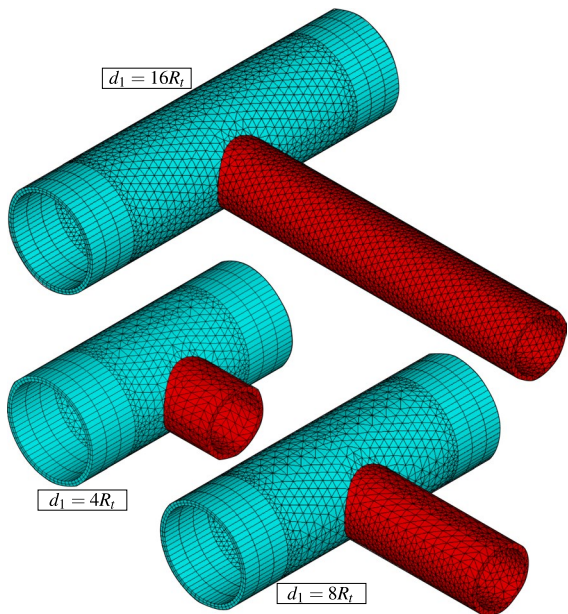


**Fig. 10** Isometric view of the lining at the intersection for  $d_1 = 16R_t$ ,  $d_1 = 8R_t$ , and  $d_1 = 4R_t$ —expansion of symmetry in the  $xz$  plane

the geometry representation of each configuration.  
It is emphasized that the tetrahedral elements used  
for the discretization of the region surrounding the

transverse gallery exactly fits excavation steps (elements removal or deactivation).

As mentioned previously, the tunnelling process, including the excavation steps and lining installation, is simulated resorting to the activation-deactivation method. Each excavation step is modeled by deactivation of the corresponding elements (the elements stiffness is reduced by a factor  $1E8$ ), whereas installation of elements of lining at a distance  $d_{0r}$  from the excavation face (unlined length) is achieved through activation of the corresponding elements by assigning them concrete properties. The F.E solution of the time-dependent problem is performed for each excavation step associated with time interval  $t_p = L_p/V_p$ , where  $L_{pt}$  represents the length of the excavation step and  $V_{pt}$  is the speed of the excavation face. Figure 11 schematically displays the consecutive phases of excavation process. In this Figure,  $n_p$  is the total number of excavation steps and  $n_{pig}$  represents the number of longitudinal tunnel excavation steps prior to gallery excavation. After achievement of the  $n_{pig}$  excavation steps, the excavation of the gallery is initiated starting from the longitudinal tunnel wall. Referring to the notation of Fig. 11,  $L_{pg}$  is the considered step length for the gallery excavation,  $V_{pg}$  is the speed of the gallery excavation, and  $d_{0g}$  is the unlined length of the gallery. Each gallery excavation step is associated with time interval  $t_{pg} = V_{pg}/L_{pg}$ . After the gallery excavation is completed, we proceed to further excavation steps of the longitudinal tunnel.

For the sake of clearness, the main parameters defining the geometry domain as well as and excavation process and lining installation are summarized in Table 1.

During the tunnel construction phases, the time increment used for the time-dependent analysis is automatically managed by the ANSYS solver. The latter makes use of a semi-implicit scheme for the viscoplasticity solution, together with an automatic time stepping algorithm (Zienkiewicz and Cormeau 1974) in which the time step is defined as a fraction of time  $t_p$  for the phases of longitudinal tunnel excavation and as a fraction of  $t_{pg}$  for the phases of transverse gallery excavation. Furthermore, distinct time steps are considered for the time-dependent analysis during tunnelling process and post-excavation stage. After complete tunnel construction phases, the analysis is carried out for a period of about 3000 days to assess the time evolving deformation as well as long-term

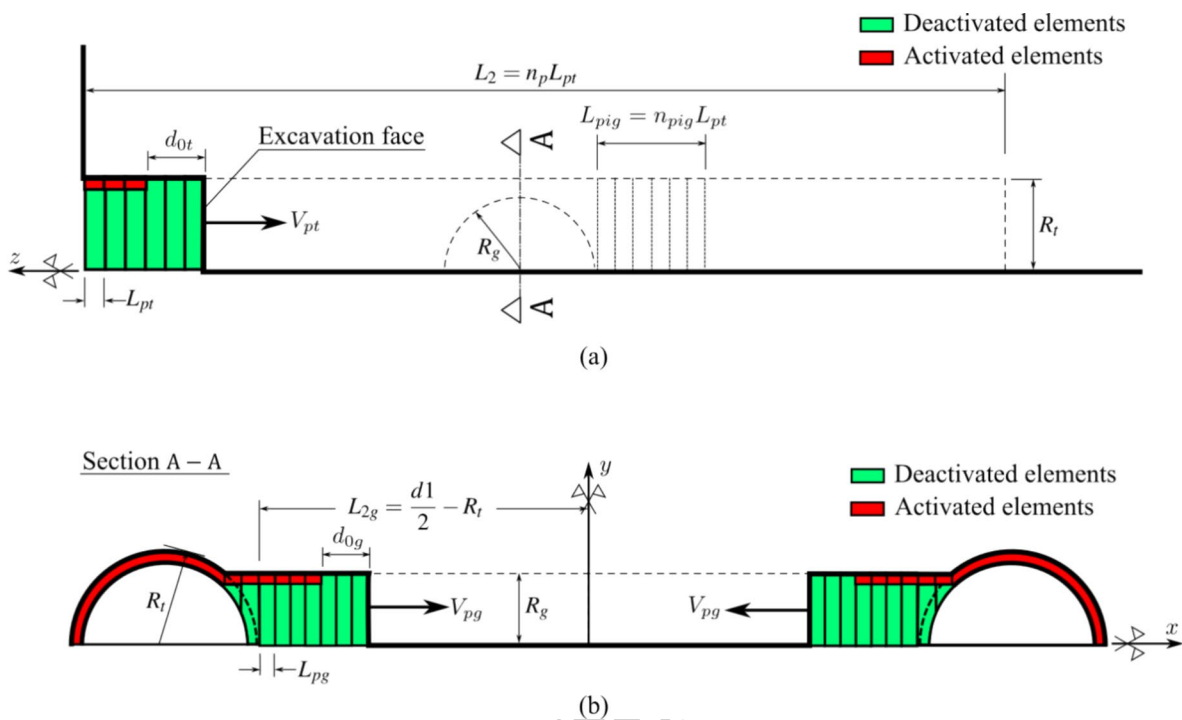


**Fig. 11** Schematic representation of the excavation and lining installation processes: **a** longitudinal tunnel; **b** transverse gallery

**Table 1** Parameters related to the geometry of the domain, excavation and installation of the lining

Parameters	Symbol	Unit	Values
<b>Longitudinal tunnels</b>			
Radius of the longitudinal tunnel	$R_t$	m	$R_t$
Thickness of the concrete lining	$e_t$	m	$0.1R_t$
Step length of the excavation process	$L_{pt}$	m	$1/3R_t$
Unlined length	$d_{0t}$	m	$2L_{pt}$
Speed of the excavation face	$V_{pt}$	m/day	12.5
Excavation step time	$t_p$	day	$L_{pt}/V_{pt}$
<b>Gallery</b>			
Radius of the gallery	$R_g$	m	$2/3R_t$
Thickness of the concrete lining	$e_g$	m	$0.1R_t$
Step length of the excavation process	$L_{pg}$	m	$1/3R_g$
Unlined length	$d_{0g}$	m	$2L_{pg}$
Speed of the excavation face	$V_{pg}$	m/day	12.5
Number of steps that starts gallery excavation	$n_{pig}$	un	15
<b>Rest of domain</b>			
Distance between longitudinal tunnel axes	$d_1$	m	$4R_t, 8R_t, 16R_t$
Thickness along vertical direction $e_y$	$d_3$	m	$20R_t$
Length of the unexcavated region	$L_1$	m	$10R_t$
Total excavated length	$L_2$	m	$100L_{pt}$
Thickness along transversal direction $e_x$	$L_3$	m	$20R_t + d_1/2$

**Table 2** Constitutive parameters of the rock material used in the numerical analysis

Parameters	Symbol	Unit	Values
Constitutive model of rock mass			
Young's modulus	$E$	MPa	1500
Poisson's ratio	$\nu$	—	0.49
Plastic cohesion	$c$	MPa	$4\sqrt{3}/2$
Plastic friction angle	$\phi$	°	0
Viscoplastic cohesion	$c_{vp}$	MPa	$2\sqrt{3}/2$
Viscoplastic friction angle	$\phi_{vp}$	°	0
Power law parameter	$n$	—	1
Reference parameter	$f_0$	MPa	1
Viscosity coefficient	$\eta$	day	40000

viscous effects on the final equilibrium of the tunnel structure. At that respect and in anticipation of the numerical results of the subsequent sections, the characteristic viscoplastic relaxation time (Simo and Hughes 1998) is equal to  $\bar{\tau} = \eta f_0/E$ , which is close to 30 days for model data of Table 2.

It should be emphasized that the twin tunnels configuration described in this section does not refer to any specific case study, but only to a typical configuration of twin deep tunnels with a transverse gallery that shall be considered in the subsequent analyses for verification and illustration purposes of the presented constitutive and computational modeling. In that respect, the geometrical parameters and material properties, such as those used in the numerical simulations of Sects. 6 and 7, are defined based on data available for deep tunnels.

## 6 Preliminary Numerical Simulations and Computational Model Verification

This section is aimed at applying the computational modeling to simulate the deformation and stress in two academic twin tunnels configurations. Both configurations address the simulation under plane strain conditions of twin tunnels without transverse gallery. The first application refers to unlined twin tunnels excavated in an elastic rock mass, whereas the second application addresses the situation of unlined twin tunnels excavated in an elastoplastic medium. Insofar as the simulations presented in the sequel do not specifically address a fully three-dimensional

configuration of twin tunnels connected by transverse gallery, the numerical results provided in these illustrative applications may be viewed only as preliminary verifications of the F.E formulation.

### 6.1 Unlined Twin Tunnels in Elastic Medium

In the context of plane strain conditions, Guo et al. (2021a, b) addressed the configuration of deep twin tunnels excavated in a homogeneous elastic medium in which prevails a hydrostatic initial stress distribution. The authors formulated approximate analytical solutions for the stress distribution establishing far behind the face, which are induced in the rock mass by the excavation of two parallel circular tunnels. The model geometry of the twin circular tunnels as well as loading associated with initial hydrostatic stress (i.e.,  $\sigma_h = \sigma_v$ ) are displayed in Fig. 12.

Simulation of the problem has been addressed by means of the 3D finite element model and the numerical results obtained for the stress distribution far behind the faces of the twin tunnel shall be compared to the analytical stress solution derived by Guo et al. (2021a, b) in the framework of plane strain conditions. The simulations have been performed taking advantage of symmetry with respect to the midplane between twin tunnels and considering the following model data: tunnel radius  $R_t = 4$  m, rock Young modulus  $E = 500$  MPa and Poisson ratio  $\nu = 0.23$ , isotropic initial stresses of  $\sigma_v = \sigma_h = 2.2$  MPa.

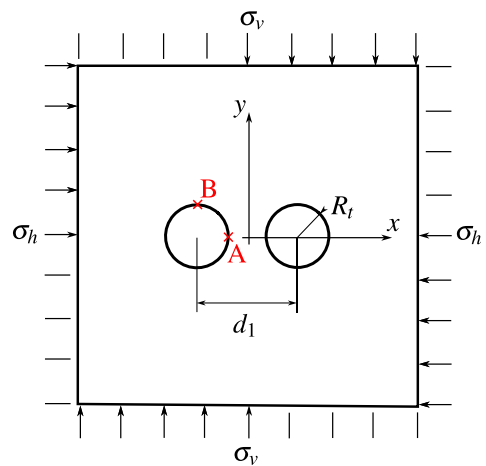
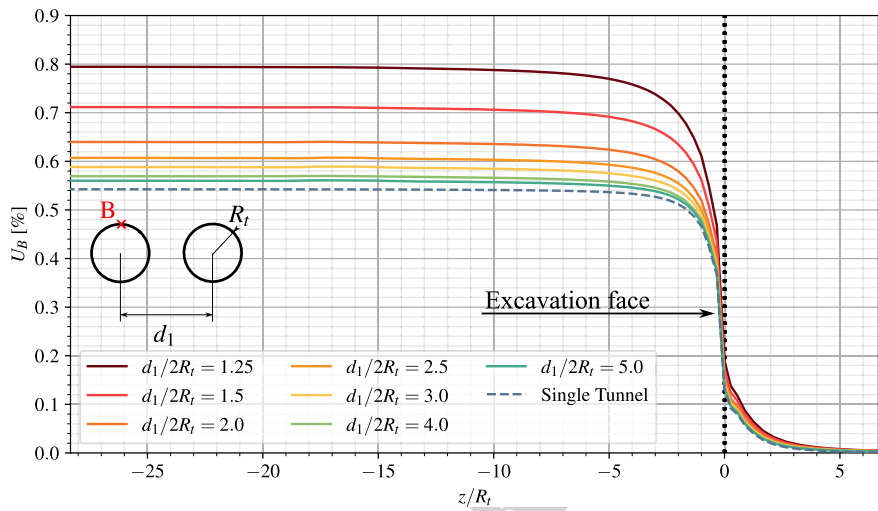


**Fig. 12** Geometry model and loading mode of the twin circular tunnels studied in Guo et al. (2021a, b)

**Fig. 13** Convergence profiles at the tunnel roof (point B)



Denoting by  $u_y$  the displacement component following the  $y$ -axis, Fig. 13 displays the convergence curves  $U_B = -u_y(B)/R_t$ , that characterize the inward movement at the tunnel roof  $B(x = -d_1/2, y = R_t, z)$  as a function of normalized longitudinal distance to the tunnel face. Several values of normalized distances between the twin tunnels axes  $d_1/2R_t$  have been investigated, and the configuration of single tunnel may be viewed as the limiting case  $d_1/2R_t \gg 1$ . It is recalled that in the latter configuration, the convergence far from the tunnel face that is obtained from an elastic analysis reads  $U = \sigma_y(1 + \nu)/E$ . As expected, this figure indicates that the closer the longitudinal tunnels, the greater the convergence at the roof.

The tunnel deformation anisotropy induced by the twin tunnels proximity is illustrated in Fig. 14, which plots the ratio  $U_B/U_A = u_y(B)/u_x(A)$  between the vertical displacement  $u_y$  at the roof B and the horizontal displacement  $u_x$  at the side wall A ( $x = -d_1/2 + R_t, y = 0, z$ ). The results shown in this figure refer to a tunnel section located far behind the face at normalized distance  $z/R_t = -25$ . They emphasize the significative tunnel ovalization induced by the proximity of twin tunnel as the distance  $d_1/2R_t$  decreases.

The stress distribution prevailing far from the tunnel face that were obtained from the 3D numerical simulations are compared in Fig. 15 to the stress solutions derived analytically and numerically in Guo

**Fig. 14** Illustration of the tunnel wall deformation anisotropy induced by twin tunnels proximity

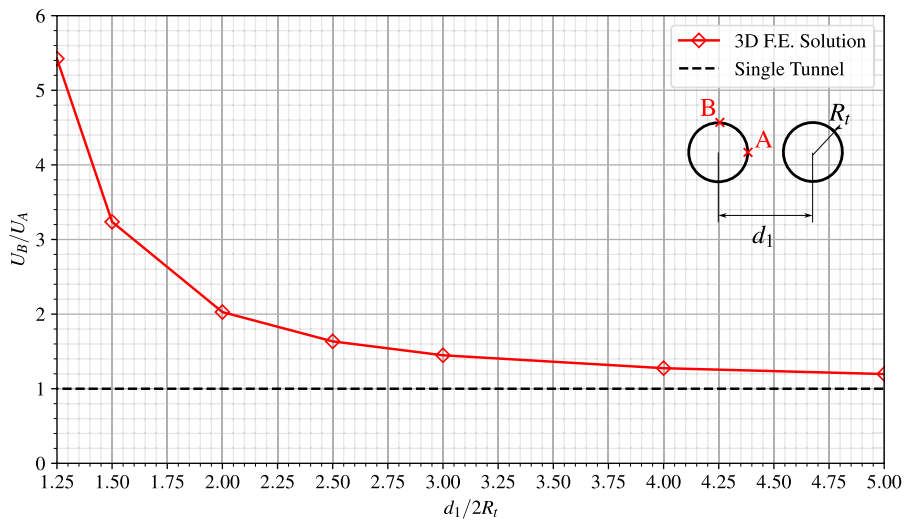
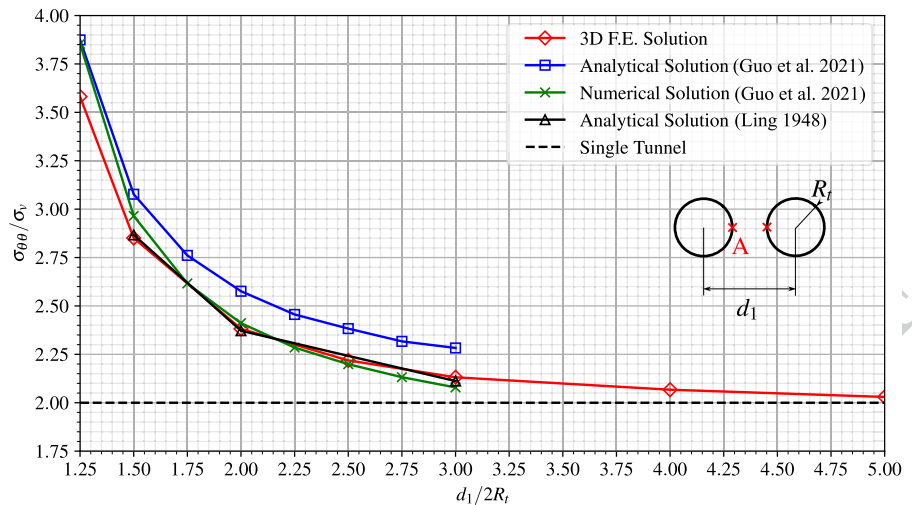


**Fig. 15** Tangential stress concentration factor at the side wall A versus twin tunnels distance  $d_1/2R_t$



et al. (2021a, b). In this figure, the tangential stress concentration factor  $\sigma_{yy}/\sigma_v$  computed at the side wall A is plotted for several values of the normalized twin tunnels distance. The results of the theoretical solution to a plate containing two circular holes of equal size presented in Ling (1948) are also reported in Fig. 15. It is observed that the results of the 3D finite element simulations correspond to a tunnel section located at normalized distance  $z/R_t = -25$  from the face, which is considered sufficient for the plane strain conditions to establish. Interestingly, the tangential stress concentration obtained for a deep single tunnel under plane strain condition simply reads  $\sigma_{yy}/\sigma_v = 2$ . Although the overall agreement observed between the different predictions, it appears from the comparison that the approximate analytical stress solution provided in Guo et al. (2021a, b) slightly overestimates the tangential stress computed at point A as the value of distance  $d_1/2R_t$  increases.

Finally, Fig. 16 displays the distribution of tangential (orthoradial) stress  $\sigma_{\theta\theta}$  around the tunnel boundary  $\{r = R_t, 0 \leq \theta \leq \pi\}$  considering  $d_1/2R_t = 1.5$ . The predictions of stress component  $\sigma_{\theta\theta}$  obtained from the 3D finite element simulations far behind the tunnel face are shown together with the strain plane solutions derived analytically in Guo et al. (2021a, b), emphasizing the ability of the computational model to accurately capture the effect of tunnels proximity on stress distribution.

Keeping in mind it addresses only an academic configuration, the results provided in this section may be viewed as a first preliminary verification of the

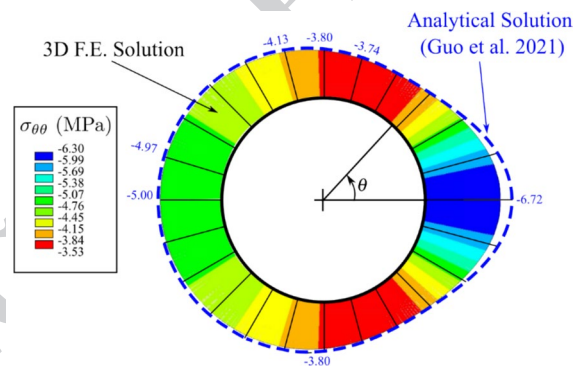


**Fig. 16** Distribution of tangential stress  $\sigma_{\theta\theta}$  around the tunnel wall prevailing far behind the tunnel face (twin tunnels distance  $d_1/2R_t = 1.5$ )

accuracy of the computational model formulated for the mechanical interaction in deep twin tunnels.

## 6.2 Unlined Twin Tunnels in Elastoplastic Medium

In the analysis developed by Ma et al. (2020), an approximate analytical solution has been formulated for the stresses and the plastic zone boundary around deep twin circular tunnels excavated in a homogeneous elastoplastic medium. The approach carried out under the assumption of plane strain condition makes use of the conformal transformation in the complex variable method to transform the solution of the elastic-plastic interfaces into the determination of the mapping function coefficients.

The geometry model and boundary loading conditions associated with the initial stress state are the same as depicted Fig. 12. Unlike the configuration studied in the preceding section, anisotropic initial stress distributions defined by  $\sigma_h \neq \sigma_v$  shall be considered in the present analysis. As regards the rock constitutive model, an elastic-perfectly plastic behavior defined by a Mohr–Coulomb criterion with associated plastic flow rule has been adopted in the study. Furthermore, the formulation of stress solution for twin tunnels configuration was based on the premise that the plastic zone around each tunnel completely encloses the tunnel edge and the two plastic zones are not connected.

For the comparison purposes, numerical simulations are carried out by means of the 3D finite element model with the aim to investigate the effect of twin tunnels proximity on the tunnel wall deformation. The following model data has been considered in the F.E. simulations: tunnel radius  $R_t = 1$  m, rock Young modulus  $E = 20$  GPa, Poisson ratio  $\nu = 0.3$ , friction angle  $\phi = 30^\circ$ , cohesion  $c = 5$  MPa or 2.5 MPa, initial vertical stress  $\sigma_v = 30$  MPa or 40 MPa, initial horizontal stress  $\sigma_h = 30$  MPa or 40 MPa. The simulation took advantage symmetry with respect to the midplane between the twin tunnels has been used for in the F.E. discretization model.

Similarly to the analysis developed in the preceding section, the convergence curves  $U_B = -u_y(B)/R_t$ , which reflects the inward movement at the tunnel roof  $B(x = -d_1/2, y = R_t, z)$ , is depicted in Fig. 17 as a function of normalized longitudinal distance to the

tunnel face. Several values of normalized distances between the twin tunnels axes  $d_1/2R_t$  have been investigated, together with the reference configuration of single tunnel, the latter being viewed as the limiting case  $d_1/2R_t \gg 1$ . As it could be expected from such simulations, this figure indicates that the proximity of tunnels significantly increases the convergence at the tunnel roof for small values, say  $d_1/2R_t < 2$ , of twin tunnel spacing. However, this effect rapidly become negligible as soon as the tunnel spacing increases.

An important feature of the twin tunnels deformation is related to the anisotropy induced by the mutual interaction as the normalized tunnel spacing  $d_1/2R_t$  decreases. In that respect, anisotropy of tunnel deformation is illustrated in Fig. 18, which presents the variations of the ratio  $U_B/U_A = u_y(B)/u_x(A)$  between the vertical displacement  $u_y$  at the roof  $B$  and the horizontal displacement  $u_x$  at the side wall  $A(x = -d_1/2 + R_t, y = 0, z)$  as a function of normalized twin tunnel spacing  $d_1/2R_t$ . These results refer to a tunnel section located far behind the face at normalized distance  $z/R_t = -35$ . As observed in the elastic case studied in the preceding section, the proximity of twin tunnels reflected by small values of normalized distance  $d_1/2R_t$  is responsible for tunnel ovalization. The magnitude of horizontal displacement at the side wall  $A$  is actually larger in than that of vertical displacement at the tunnel roof  $B$ , thus indicating an ovalization in the vertical direction (i.e., parallel to  $y$ -axis).

**Fig. 17** Convergence profiles at the tunnel roof (point B);  $c = 5$  MPa,  $\sigma_v = \sigma_h = 30$  MPa

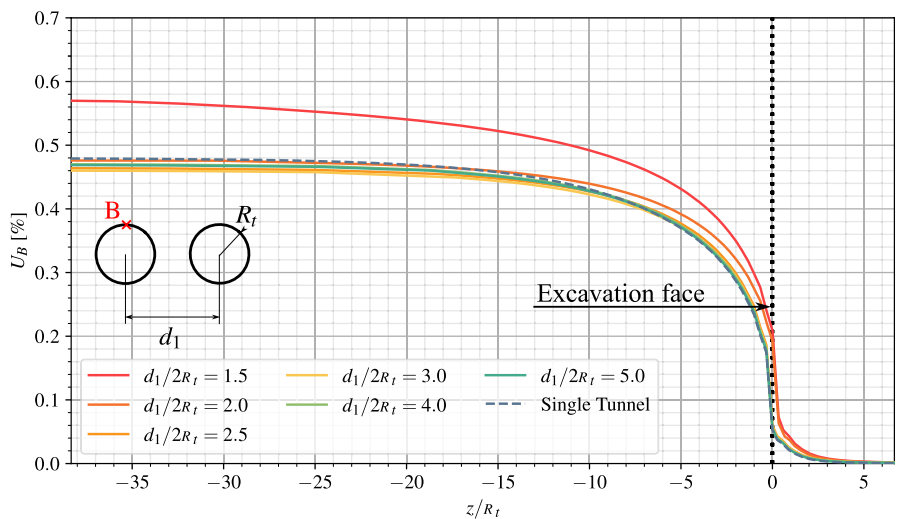


**Fig. 18** Tunnel wall deformation anisotropy induced by twin tunnels proximity:  $c = 5 \text{ MPa}$ ,  $\sigma_v = \sigma_h = 30 \text{ MPa}$

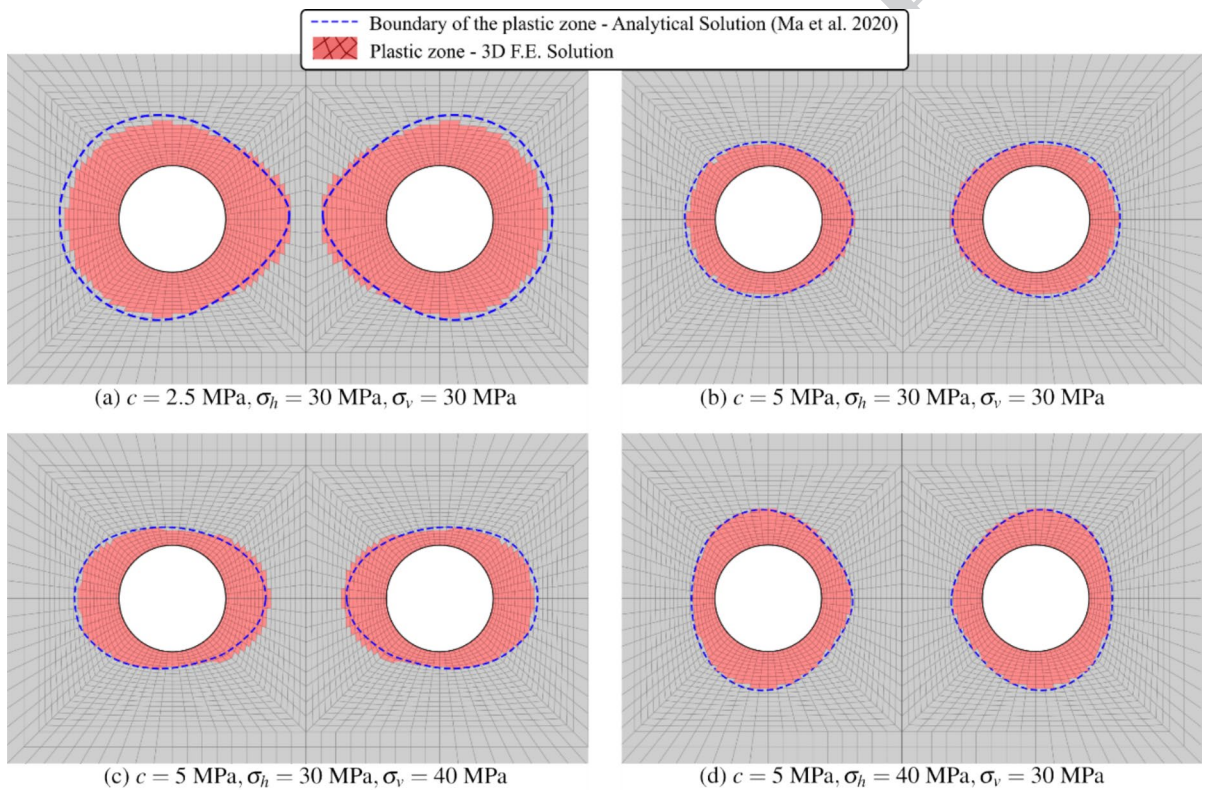
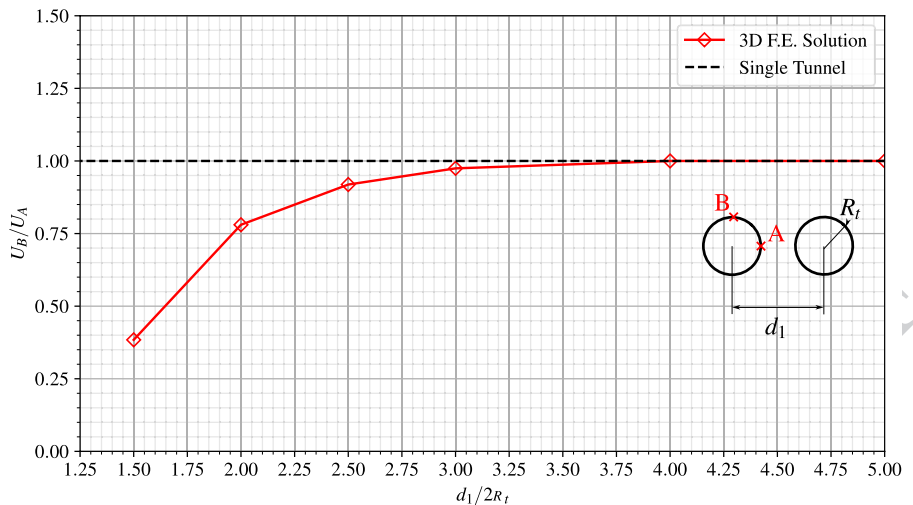


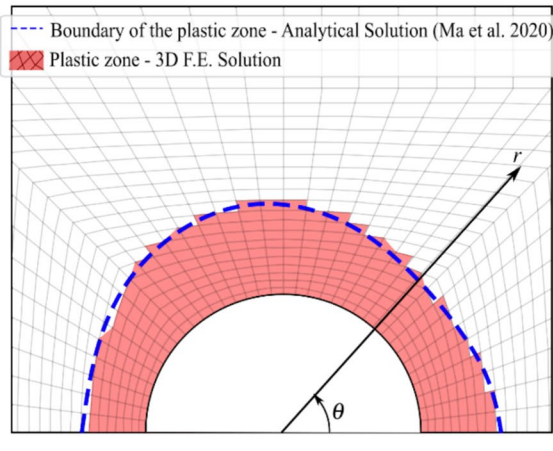
**Fig. 19** Plastic zone extent obtained from the present F.E. simulations and from the stress solution provided in Ma et al. (2020)

930 The stress distribution prevailing far from the  
931 tunnel face that were obtained from the 3D numeri-  
932 cal simulations are compared in the to the approx-  
933 imate stress solutions derived by Ma et al. (2020)  
934 within the context of plane strain conditions.

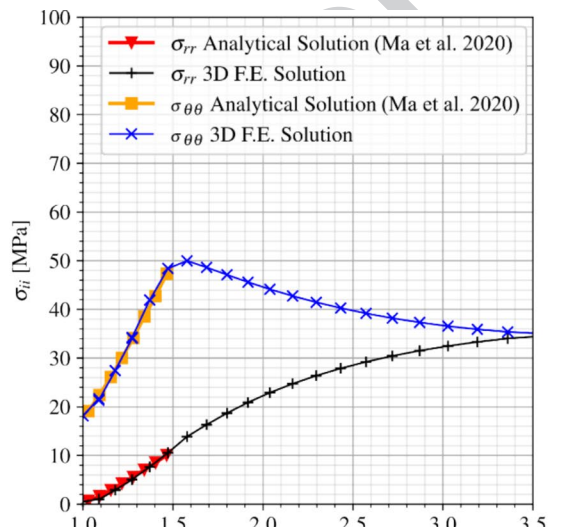
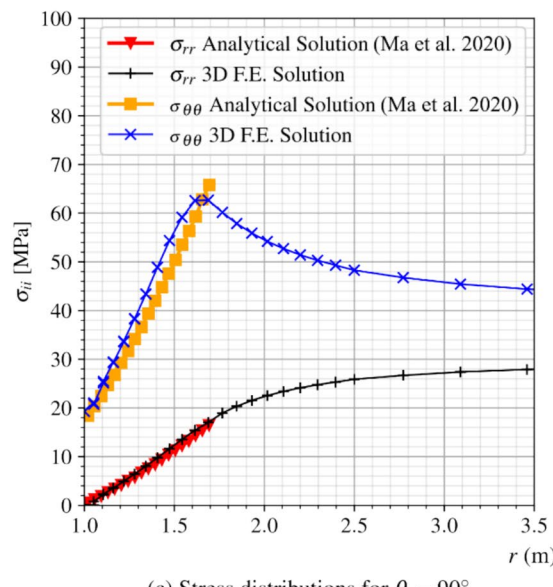
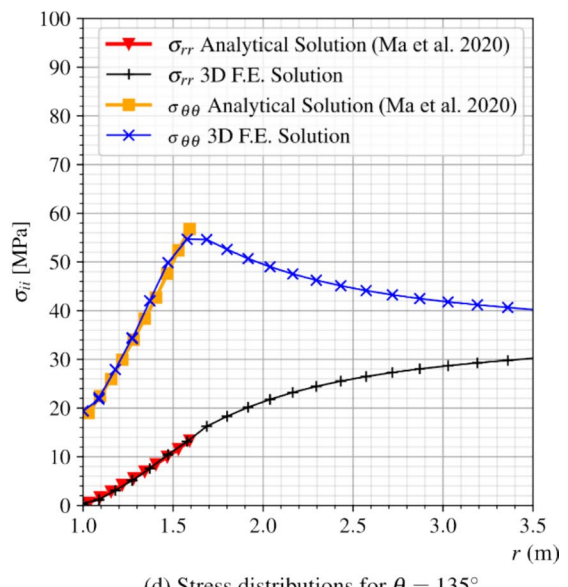
Figure 19 displays such a comparison in terms of  
935 predicted plastic zone surrounding the twin tun-  
936 nels considering a normalized tunnel spacing of  
937  $d_1/2R_t = 2.5$ . Different values have been considered  
938 for rock cohesion  $c$  and initial stresses  $\sigma_v$  and  $\sigma_h$ . It  
939

940 appears from the latter figure that the finite element  
 941 modeling produces predictions very similar to those  
 942 provided in Fig. 19. The results also illustrate that  
 943 larger plastic zones arise when the cohesion  $c$  is  
 944 smaller.

Further comparisons are shown in Fig. 20, which  
 945 presents the plots of radial  $\sigma_{rr}$ , and orthoradial  $\sigma_{\theta\theta}$   
 946 stress components along three radial paths defined  
 947 in polar coordinates by  $\theta = 45^\circ, 90^\circ$  and  $135^\circ$ . It  
 948 should be pointed out that, although the F.E. element  
 949 simulations make use of the Drucker-Prager yield  
 950 surface inscribed to the Mohr-Coulomb one, used  
 951



(a) Plastic zone extent

(b) Stress distributions for  $\theta = 45^\circ$ (c) Stress distributions for  $\theta = 90^\circ$ (d) Stress distributions for  $\theta = 135^\circ$ 

**Fig. 20** Plastic zone extent and distribution of radial and orthoradial stresses along different radial directions: comparison between numerical and analytical predictions ( $d_1/2R_t = 2.5$ ,  $E = 20$  GPa,  $v = 0.3$ ,  $c = 5$  MPa,  $\phi = 30^\circ$ ,  $\sigma_h = 40$  MPa,  $\sigma_v = 30$  MPa)

952 in the solution of Ma et al. (2020), the numerical  
 953 predictions are matching well with the analytical  
 954 stress solution.

## 955 7 Three-Dimensional Finite Element Simulations

956 This section provides some numerical results related  
 957 to rock deformation in twin tunnels with transverse  
 958 gallery obtained from the 3D computational model  
 959 presented in Sects. 3, 4 and 5. It is emphasized that  
 960 the primary objective herein is to illustrate the capa-  
 961 bilities of the proposed formulation to address within  
 962 a 3D context the configuration of a complex tunnel  
 963 structure involving nonlinear and time-dependent  
 964 couplings. Elaboration of an exhaustive parametric  
 965 analysis integrating the effects of geometrical, consti-  
 966 tutive and loading parameters is notably beyond the  
 967 scope of the numerical application.

### 968 7.1 Model Data and Preliminary Considerations

969 The rock constitutive data used in the subsequent  
 970 analysis refer to a deep clay from eastern Paris basin  
 971 (Aisne region, France) studied in Rousset (1988),  
 972 Giraud and Rousset (1996), Piepi (1995), Giraud  
 973 (1993). The material properties including elasto-  
 974 plastic and viscoplastic parameters summarized in  
 975 Table 2 have been evaluated and calibrated from an  
 976 extensive series of laboratory tests performed under

undrained conditions (Rousset 1988; Piepi 1995;  
 977 Giraud 1993). The Aisne clay rocks exhibit high den-  
 978 sity (2.01 to 2.57 g/cm<sup>3</sup>), a low average water con-  
 979 tent (between 3 to 11%) and relatively low porosity  
 980 (typically less than 20%). It is therefore assumed that  
 981 hydromechanical coupling can be neglected in the  
 982 analysis of rock material deformation. In particular,  
 983 the creep tests indicated that the long-term effects pri-  
 984 marily stem from material viscosity, with a very low  
 985 proportion induced by pore pressure redistribution.  
 986 An important characteristic of the behavior such clay  
 987 is that irreversible strains are observed in cyclic tests  
 988 even at small values of axial strain (less than 0.3%).  
 989 The instantaneous undrained triaxial tests performed  
 990 at high confining pressure values, such as those pre-  
 991 vailing in the rock mass at approximately 450 m deep,  
 992 indicated that the maximum deviatoric stress remains  
 993 approximately constant, thus suggesting a Tresca-  
 994 type failure criterion for the short-term component of  
 995 the behavior. As for the long-term behavior, the creep  
 996 tests revealed that the deviatoric stress threshold  
 997 beyond which the material exhibits creep deformation  
 998 is almost independent on the mean stress, suggest-  
 999 ing that the time-dependent behavior component can  
 1000 be conveniently described by a Tresca-like criterion.  
 1001 Comparison of instantaneous and delayed behaviors  
 1002 reveals that short-term cohesion exceeds long-term  
 1003 cohesion within a ratio ranging between 1.2 and 2.  
 1004 Based on these observations, the constitutive model  
 1005 data adopted for the elastoplastic and viscoplastic  
 1006

**Table 3** Constitutive and geometric parameters of the support systems used in the numerical analysis

Parameters	Symbol	Unit	Values
Constitutive model of lining			
Characteristic compressive strength at age of 28 days	$f_{ck}$	MPa	20
Modulus of elasticity at the age of 28 days	$E_{c_{28}}$	MPa	30303
Poisson's ratio	$\nu_c$	—	0.2
Coefficient defining instantaneous relaxation modulus (1993)	$s$	—	0.2
Relative humidity of ambient environment	$RH$	%	70
Notional size of member—longitudinal concrete lining	$h_l$	cm	0.2111
Notional size of member—gallery concrete lining	$h_g$	cm	0.2176
Age of concrete at the beginning of shrinkage	$t_s$	days	7
Shrinkage coefficient depending on cement type (1993)	$\beta_{sc}$	—	8
Temperature	$T$	°C	20
Age of concrete at loading	$t_0$	days	1
Geometric parameter			
Thickness of the tunnel lining	$e_t$	m	$0.1R_t$
Thickness of the gallery lining	$e_g$	m	$0.1R_t$

1007 components of the rock material behavior is summarized in Table 2.

1009 Table 3 provides the reference constitutive parameters and thickness of the lining support systems of  
 1010 the tunnels and transverse gallery that will be considered in the numerical simulations. The instantaneous  
 1011 relaxation modulus under uniaxial stress at 28 days  
 1012 being referred to as  $E_{c_{28}}$ . In the analyses that consider elastic behavior of the lining, the concrete elastic  
 1013 modulus is set equal to  $E_{c_{28}}$ . When viscoelastic behavior is adopted for the lining, the relaxation modulus  
 1014 evolves in time according to the Generalized Kelvin  
 1015 model described in Sect. 4, whereas the Poisson ratio  
 1016 is assumed to be constant within the time interval  
 1017 of analysis. During the tunnel construction process,  
 1018 loading and creep of each lining segment starts from  
 1019 the moment it is activated with properties at age  
 1020  $t_0 = 1$  day, whereas shrinkage effects are assumed to  
 1021 take part at the age of  $t_s = 7$  days.

1022 The parameters defining the structure geometry as  
 1023 well as the excavation and lining installation process  
 1024 are provided in Table 1. All the length parameters are  
 1025 normalized by the tunnel radius  $R_t$ , which amounts  
 1026 to formally consider radius  $R_t = 1$  m in the numerical  
 1027 simulations. As mentioned in Table 1, three different  
 1028 values shall be considered in the simulations  
 1029 for the distance between twin tunnels axes, namely  
 1030  $d_1 = 4R_t$ ,  $d_1 = 8R_t$ , and  $d_1 = 16R_t$ . In addition, con-  
 1031 stant values of tunnel and gallery advancement rates  
 1032 are considered and fixed to  $V_{pt} = V_{pg} = 12.5$  m/day.  
 1033 As regards the initial stress state prevailing prior to  
 1034 excavation processes, hydrostatic stress distribution  
 1035 with  $\sigma_v = \sigma_h = 9$  MPa, corresponding to geostatic  
 1036 conditions at depths of about of 450 m, is adopted  
 1037 in the subsequent simulations. The numerical study  
 1038 investigates the long-term and short-term tunnel con-  
 1039 vergence profiles considering various constitutive  
 1040 models for the rock mass (elastic, elastoplastic, vis-  
 1041 coplastic or elastoplastic-viscoplastic) and for the lin-  
 1042 ing (elastic and viscoelastic). For the comparison pur-  
 1043 poses, the configuration of unlined tunnel as well as  
 1044 the configurations with or without transverse gallery  
 1045 will also be analyzed. To facilitate the description of  
 1046 the different configurations addressed below, Table 4  
 1047 provides the list of each configuration as well as asso-  
 1048 ciated abbreviation used to refer to in the presentation  
 1049 of numerical results.

1050 Denoting by  $u_y$  the displacement component  
 1051 along the vertical y-axis, all the results presented

**Table 4** Configurations and associated abbreviations used in numerical simulations

Description	Abbreviation
Elastic rock mass	E
Elastoplastic rock mass	EP
Elastoviscoplastic rock mass	VP
Elastoplastic-Viscoplastic rock mass	EPVP
No lining	NL
Elastic lining	EL
Viscoelastic lining	VEL
Long-term	LT
End of excavation process (Short-term)	ST
With gallery	WG
No gallery	NG

1052 in the following analyses will specifically refer  
 1053 to the convergence profile  $U_B = -u_y(B)/R_t$  that  
 1054 characterizes the inward movement of the tun-  
 1055 nel roof  $B(x = -d_1/2, y = R_t, z)$  as a function of  
 1056 the normalized algebraic longitudinal distance  
 1057  $z/R_t$  from the excavation face. In addition, point  
 1058  $C(x = -d_1/2, y = R_t, z = -25R_t)$  has been chosen  
 1059 as representative of the equilibrium convergence  
 1060  $U_C$  far behind the tunnel face and transverse gallery.  
 1061 When the gallery intersects the longitudinal tun-  
 1062 nel, the highest convergence value  $U_{peak}$  highlighted  
 1063 in the plots of convergence curves refers to point  
 1064  $D(x = -d_1/2, y = R_t, z = L_1 + L_2/2)$  located at the  
 1065 roof of longitudinal tunnel section lying at the tun-  
 1066 nel/transverse gallery junction.

1067 The first feature of tunnel deformation to be men-  
 1068 tioned is related to the tunnel deformation anisotropy  
 1069 (or ovalization) induced by the twin tunnels proxim-  
 1070 ity. A single circular tunnel excavated in a homoge-  
 1071 neous isotropic rock mass with hydrostatic initial stress  
 1072 state will deform symmetrically so that the circular  
 1073 shape of tunnel wall will be preserved throughout  
 1074 the excavation process. As already pointed out in  
 1075 the preliminary numerical simulations presented in  
 1076 Sect. 6, the mutual interaction associated with twin  
 1077 tunnels proximity will in contrast result in anisotropic  
 1078 deformation of the tunnel wall, the ovalization effect  
 1079 being more pronounced as the distance between twin  
 1080 tunnels axes  $d_1$  decreases. For illustrative purposes,  
 1081 Fig. 21 presents schematic plots of the deformed tun-  
 1082 nel wall far behind the face together with trajectory of  
 1083 monitoring point B considering three different values  
 1084 of  $d_1$ .

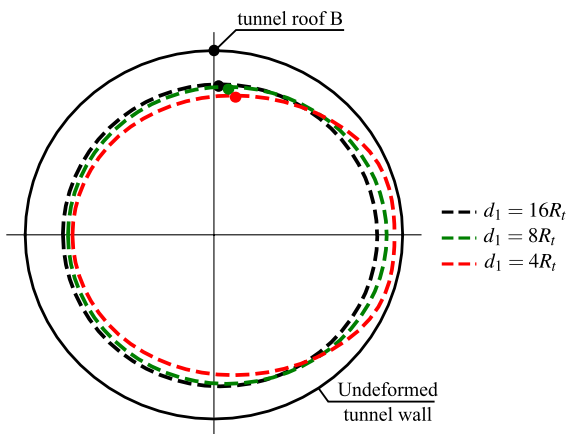


**Fig. 21** Illustration of the deformation anisotropy induced by twin tunnels proximity

of normalized twin tunnel spacing  $d_1/R_t$ . The configuration shown in this figure corresponds to elastoplastic rock mass (EP), elastic lining (EL) and transverse gallery (WG). It should be however kept in mind that due to tunnel ovalization,  $U_B$  would not be therefore sufficient for characterizing the whole deformation of the tunnel wall.

The second feature of the tunnel deformation that deserves to be mentioned refer the specific deformation patterns prevailing in the region surrounding the tunnel wall. In consistence with experimental data, the plastic cohesion  $c$  and viscoplastic cohesion  $c_{vp}$

reported in Table 2 comply with condition  $c > c_{vp}$ . This notably implies that irreversible viscoplastic strains will be activated earlier as the tunnel excavation. Schematic representation of deformation patterns within the rock mass is illustrated in Fig. 22.

## 7.2 Short and Long-Term Convergence Profiles

Figures 23, 24 and 25 show the convergence profiles in the twin tunnels with gallery (WG) considering the different constitutive models of the rock mass (E—blue, EP—yellow, VP—magenta, EPVP—red and green) and of the lining (EL and VEL). The interaction effect rising from twin tunnels proximity is investigated by considering three values  $d_1 = 4R_t$ ,  $d_1 = 8R_t$ , and  $d_1 = 16R_t$ . The solid lines refer to short-term analysis (ST) whereas the dashed lines to long-term analysis (LT).

For all investigated values of twin tunnels distance  $d_1$ , the convergence profiles obtained in short-term (ST) analyses are very similar for both the E-EL (blue dashed line) and the VP-EL (magenta solid line) constitutive model configurations. This mainly attributed to relatively high value considered for the tunnel/gallery advancement rate and lining installation (excavation speed  $V_{pt} = V_{pg}$ ), thus limiting the viscous effects on the tunnel deformation. The same explanation holds regarding the results derived from the short-term (ST) analyses with the EP-EL (yellow dashed line) or EPVP-EL (green

**Fig. 22** Evolution of deformation zones as the tunnel excavation proceeds

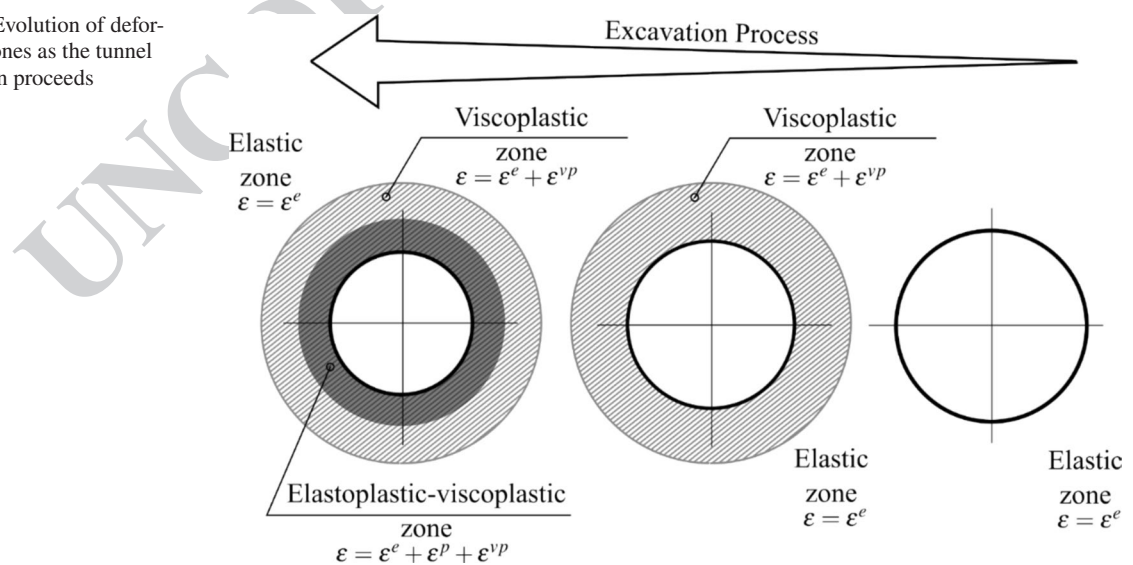


**Fig. 23** Convergence Profiles: short-term (ST) and long-term (LT) analyses for the configuration with gallery (WG) and distance between twin tunnels  $d_1 = 16R_t$

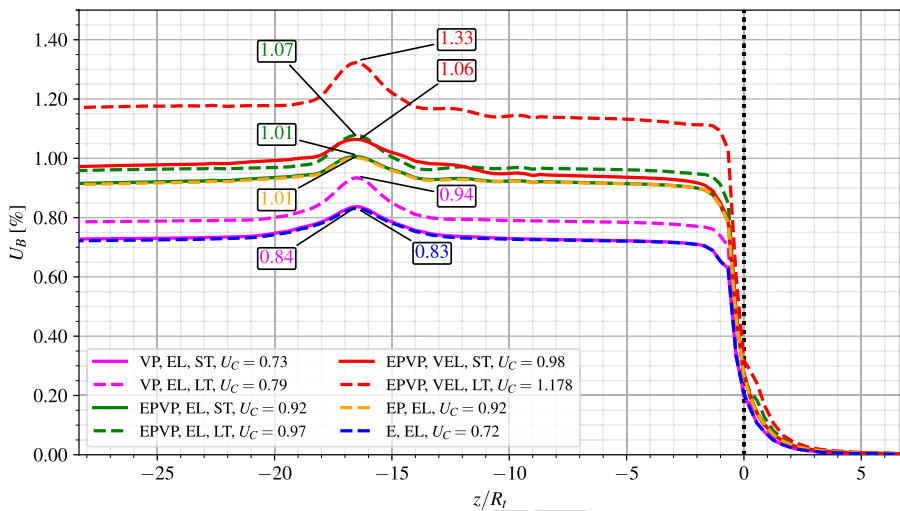


**Fig. 24** Convergence Profiles: short-term (ST) and long-term (LT) analyses for the configuration with gallery (WG) and distance between twin tunnels  $d_1 = 8R_t$

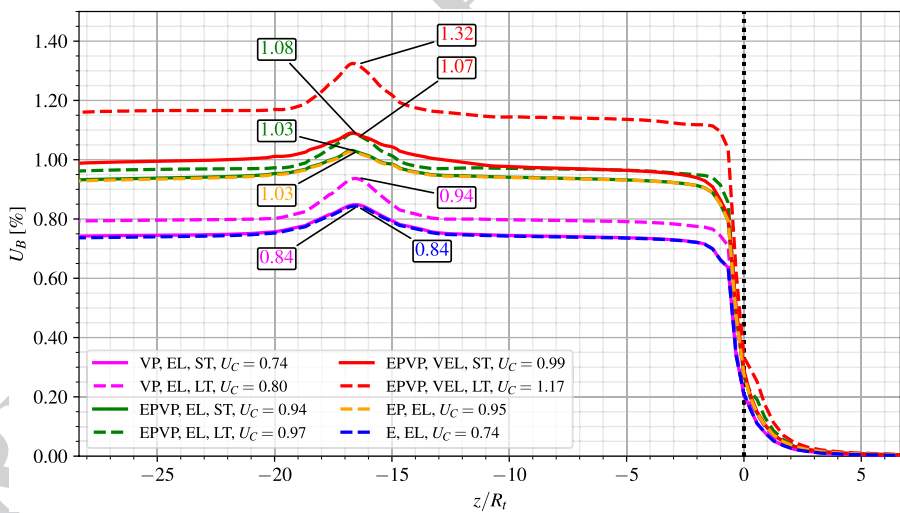
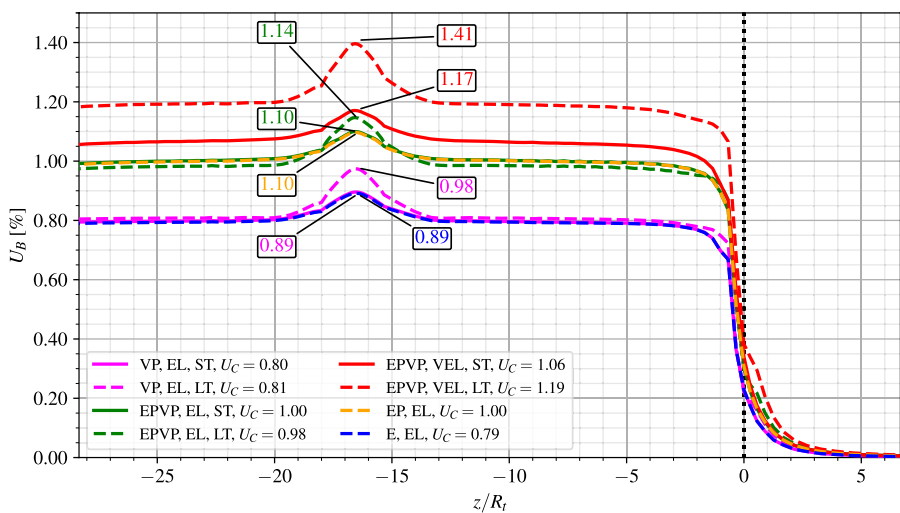


**Fig. 25** Convergence Profiles: short-term (ST) and long-term (LT) analyses for the configuration with gallery (WG) and distance between twin tunnels  $d_1 = 4R_t$



solid line) constitutive model configurations. However, the viscous effects give rise to delayed tunnel deformation progressively affecting the long-term (LT) convergence (dashed green line) at the tunnel roof B. The discrepancy between short-term and long-term responses is more pronounced when a time-dependent viscoelastic lining is considered, as clearly indicated from the convergence associated with the EPVP-VEL model (solid and dashed red lines).

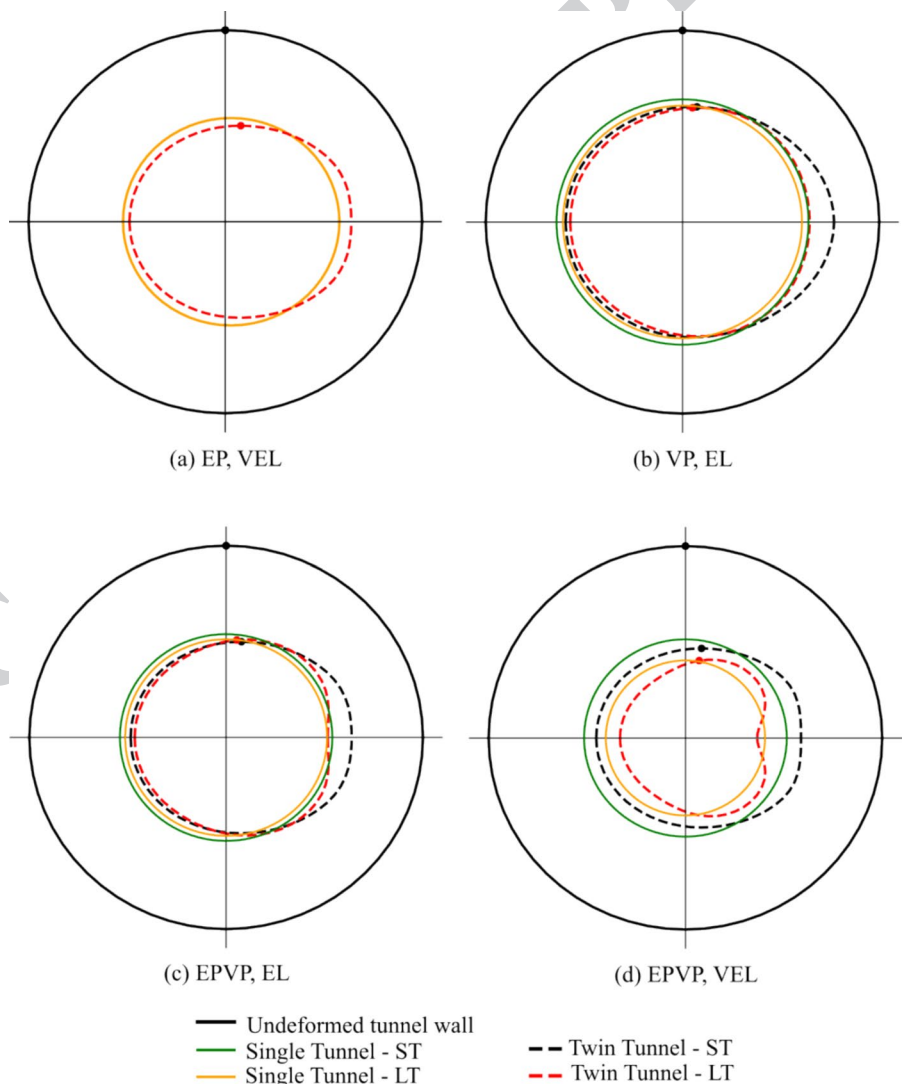
It is noted that the relatively high stiffness considered of the elastic lining is likely to significantly reduce the viscous component of tunnel wall deformation. This can be illustrated by analyzing the short-term and long-term convergences for VP-EL model

(solid and dashed magenta line). In this configuration, the twin tunnels proximity induces a substantial increase in the short-term (ST) prediction of  $U_C$  when comparing  $d_1 = 8R_t$  and  $d_1 = 4R_t$ , whereas the long-term (LT) convergence hardly changes mainly due to the restriction imposed by the stiff lining.

Referring to the configuration analyzed in Figs. 23, 24 and 25, the ovalization effect may be illustrated by visualizing in Fig. 26 the anisotropic deformation of a tunnel cross-section located far behind the face in the particular case of twin tunnel distance  $d_1 = 4R_t$ . In this figure, the configuration of a single circular tunnel ( $d_1 \rightarrow \infty$ ) is also shown as a reference case.

In that respect, Fig. 27 provides further illustration of the ovalization effect by plotting the

**Fig. 26** Illustration of the deformation anisotropy induced by twin tunnels proximity: configuration with gallery (WG) and distance between twin tunnels  $d_1 = 4R_t$



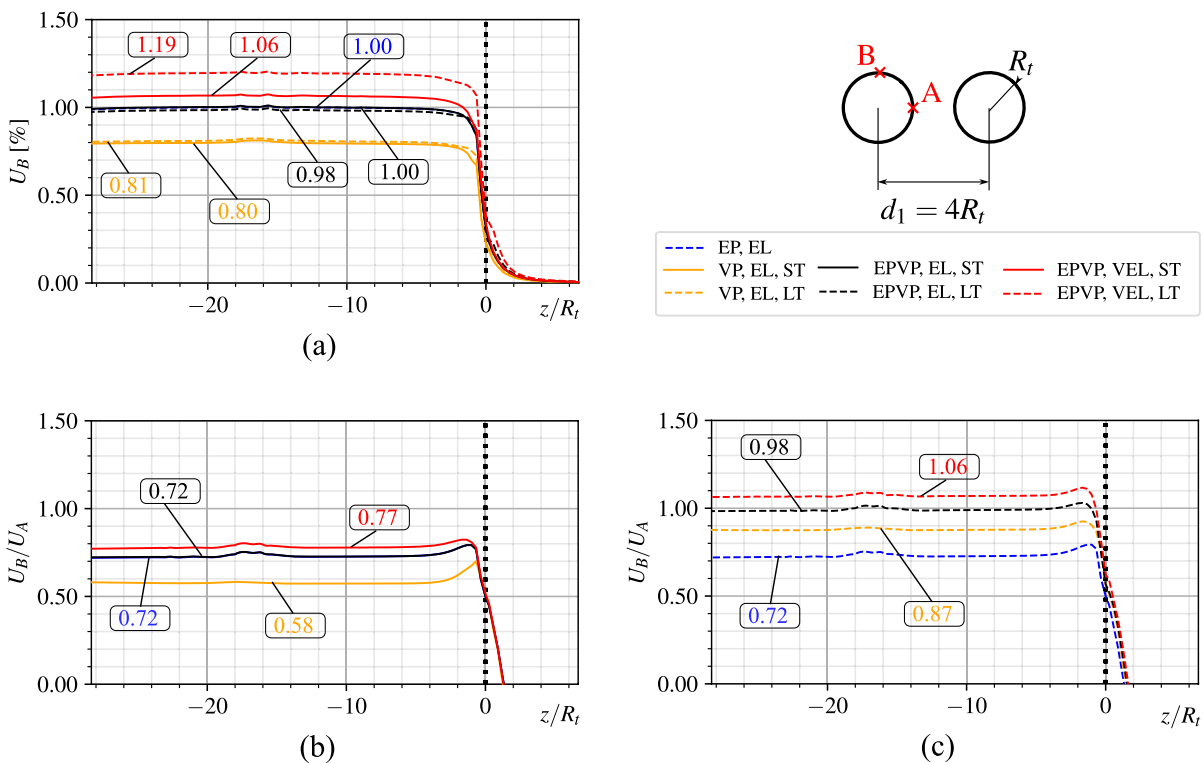
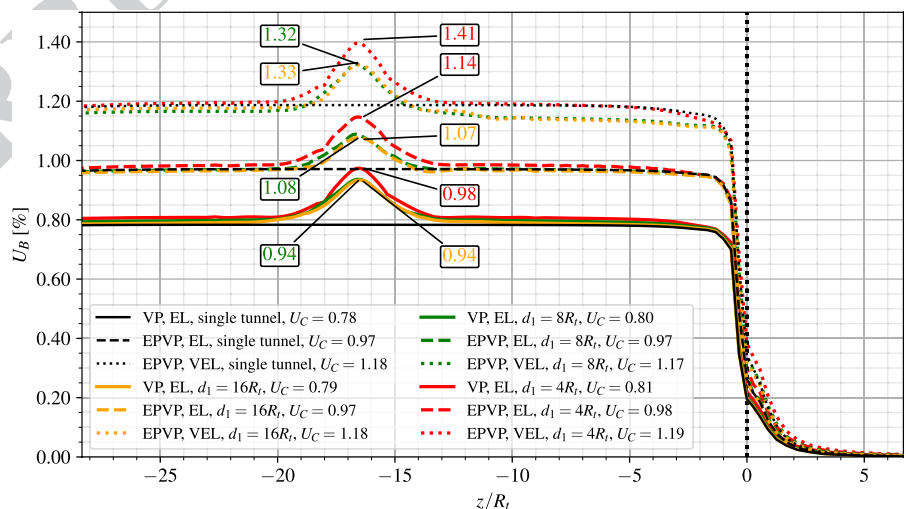


**Fig. 27** Deformation anisotropy induced by twin tunnels proximity for the configuration without gallery (NG) and distance between twin tunnels  $d_1 = 4R_t$ ; **a** convergence profile at the

tunnel roof B; **b** anisotropy ratio obtained in short-term analysis; **c** anisotropy ratio obtained in long-term analysis

**Fig. 28** Long-term convergence profiles for the configuration of twin tunnels with transverse gallery (WG): effect of rock mass and lining creep deformation



1158 anisotropy ratio  $U_B/U_A = u_y(B)/u_x(A)$  between  
1159 the vertical displacement  $u_y$  at the roof B and

the horizontal displacement  $u_x$  at the side wall 1160  $A(x = R_t - d_1/2, y = 0, z)$ . The resulted presented in 1161 this figure correspond to twin tunnels without trans- 1162 verse gallery (NG) and distance  $d_1 = 4R_t$ . The results 1163

1164 suggest a more pronounced ovalization effect short-  
1165 term tunnel deformation (solid lines).

### 1166 7.3 Additional Numerical Analyses: Impact of Creep 1167 Deformation

1168 This section provides further numerical results  
1169 obtained from long-term and short-term analy-  
1170 ses, with particular emphasis on the effect of time-  
1171 dependent behavior of the rock material and lining  
1172 constituent materials. Figure 28 displays the long-  
1173 term convergence profiles for  $d_1 = 16R_t$ ,  $8R_t$  and  $4R_t$   
1174 (yellow, green and red lines, respectively) consider-  
1175 ing viscous constitutive models: viscoplastic rock mass  
1176 with elastic lining (VP-EL—solid lines), elastoplas-  
1177 tic-viscoplastic rock mass with elastic lining (EPVP-  
1178 EL—dashed line) and viscoelastic lining (EPVP-  
1179 VEL—dotted lines). To emphasize the interaction  
1180 rising from twin tunnels proximity and transverse gal-  
1181 lery, the results obtained in the reference configura-  
1182 tion of a single tunnel (black lines) are also shown.  
1183 Close values of the peak convergence  $U_{peak}$  are  
1184 obtained at the tunnel roof for the EPVP-VEL model  
1185 with  $d_1 = 16R_t$  (yellow dotted line) and with  $d_1 = 8R_t$   
1186 (green dotted line). This result may be explained by  
1187 the fact the overall interaction effect on tunnel conver-  
1188 gence results from the competing effects of twin tun-  
1189 nel proximity (defined by  $d_1$ ) and the time necessary  
1190 for complete gallery excavation and its intersection  
1191 with longitudinal tunnel (also defined by length by  
1192  $d_1$ ). The results indicated that these competing phe-  
1193 nomena lead to equivalent overall effect in the cases

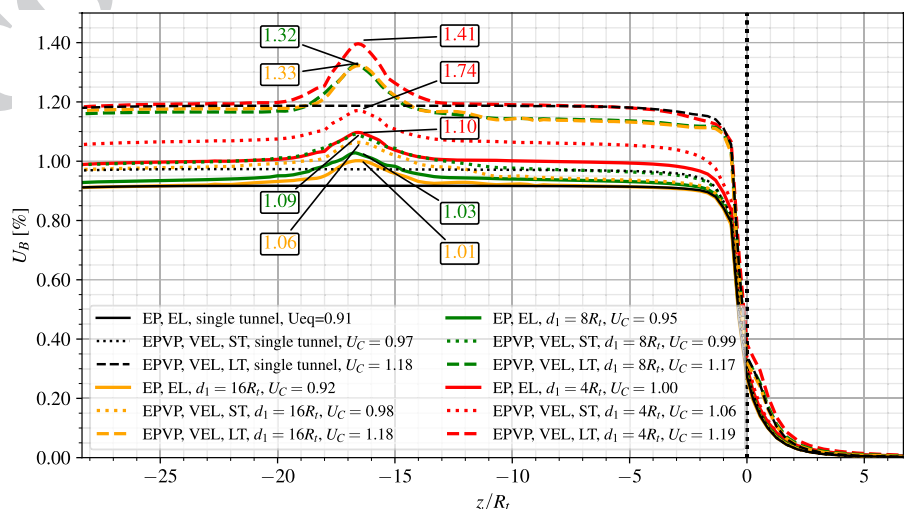
of  $d_1 = 8R_t$  and  $d_1 = 16R_t$ . In the case of  $d_1 = 4R_t$   
1194 (red dotted line), the effect of twin tunnel proxim-  
1195 ity appears to be predominant, which lead to higher  
1196 value of the peak convergence  $U_{peak}$ .  
1197

Referring to EPVP-VEL and EPVP-EL models  
1198 (dotted lines and dashed lines), it can be seen from  
1199 the results of Fig. 28 that higher convergence values  
1200 are associated with time-dependent behavior of the  
1201 lining. Unlike the stiff elastic lining, the aging vis-  
1202 coelastic lining induces evolving tunnel convergence  
1203 along the excavation process.  
1204

The impact of creep deformation on the tunnel  
1205 convergence can alternatively be illustrated based on  
1206 the comparison of the numerical predictions obtained  
1207 in the cases of instantaneous behavior (elastoplas-  
1208 tic, elastic) and time-dependent behavior (viscoplas-  
1209 tic, viscoelastic) for the constituent materials. Fig-  
1210 ure 29 depicts the convergence profiles obtained for  
1211  $d_1 = 16R_t$ ,  $8R_t$  and  $4R_t$  (yellow, green and red lines,  
1212 respectively) considering the configurations of elas-  
1213 toplastic rock mass with elastic lining (EP-EL—solid  
1214 lines), elastoplastic-viscoplastic rock mass with vis-  
1215 coelastic lining in short-term analysis (EPVP-VEL-  
1216 ST—dotted lines) and elastoplastic-viscoplastic rock  
1217 mass with viscoelastic lining in long-term analysis  
1218 (EPVP-VEL-LT—dashed lines). The case of single  
1219 circular tunnel ( $d_1 \rightarrow \infty$ ) is also analyzed as reference  
1220 configuration (black lines).  
1221

Once again, the result predictions shown in this  
1222 figure emphasize the significative impact of the vis-  
1223 coelastic lining behavior on the short-term conver-  
1224 gence profile of the tunnels. At short-term (ST), the  
1225

**Fig. 29** Short-term and long-term convergence profiles obtained for the configuration of twin tunnels with transverse gallery (WG): instantaneous versus delayed behaviors of the rock and lining constituent material



1226 elastoplastic-viscoplastic rock mass with viscoelastic lining (EPVP-VEL—dotted lines) leads to higher  
 1227 convergences when compared to the elastoplastic rock mass with elastic lining (EP-EL—solid lines). This is  
 1228 mainly attributed to the fact the early age viscoelastic lining (VEL) exhibits lower relaxation modulus than  
 1229 the stiffness  $E_{c_{28}}$  considered for elastic lining (EL),  
 1230 thus resulting in higher tunnel deformation. Regarding  
 1231 the long-term analysis (LT), even though the viscoelastic lining (VEL) (dashed lines) exhibit increasing  
 1232 relaxation modulus due to aging phenomenon, the  
 1233 creep deformation of both the rock and lining constituents result in significantly higher convergences at  
 1234 the tunnel roof when compared to obtained for elastoplastic rock with elastic lining (EP-EL—solid lines).  
 1235 A noticeable increase in the magnitude of  $U_{peak}$ ,  
 1236 induced by the interaction with transverse gallery,  
 1237 is also observed from the short-term response (dotted lines) to the long-term response (dashed lines),  
 1238 highlighting once again the influence of the delayed  
 1239 behavior of the rock and the lining.  
 1240

#### 1241 7.4 Effect of the Lining Stiffness on the Tunnel 1242 Convergence

1243 In tunnel deformation analyses, the behavior of the concrete lining is classically characterized by the elastic stiffness parameter, which relates the normal stress exerted by the surrounding the rock mass and the normalized lining normal displacement (convergence). The elastic stiffness parameter is computed

1244 from the elastic properties of concrete material and the lining thickness (normalized by the tunnel radius)  
 1245 (Panet 1995; Hoek and Brown 1980). This concept  
 1246 is extended herein to case of viscoelastic lining by  
 1247 in traducing the instantaneous stiffness modulus at  
 1248 28 days  $K_{c_{28}}$  as:  
 1249

$$1250 K_{c_{28}} = \frac{E_{c_{28}}}{1 + \nu_c} \frac{1 - (1 - e_t/R_t)^2}{(1 - 2\nu_c) + (1 - e_t/R_t)^2} \quad (18)$$

1251 In the above analyses of Sects. 7.1, 7.2 and 7.3 the lining thickness were fixed to  $e_t = e_g = 0.1R_t$ , corresponding to lining stiffness  $K_{c_{28}} = 3400$  MPa. As far as the tunnel deformation is concerned, the latter value characterizes a rather stiff lining, which might be a predominating factor for the control of tunnel convergence.

1252 To assess the effect of the lining stiffness on the convergence profile, a smaller value  $e_t = e_g = 0.03R_t$ , corresponding to lining stiffness modulus  $K_{c_{28}} = 970$  MPa, will be in the numerical simulations. Referring to the particular case of a rock mass exhibiting elastoplastic behavior (EP), that is only instantaneous behavior, Figs. 30 and 31 display the convergence profiles at tunnel roof predicted respectively for  $d_1 = 16R_t$  and  $d_1 = 4R_t$ . Three configurations for the support lining are considered: unlined structure (NL—dashed lines), elastic lining with lower stiffness  $K_{c_{28}} = 970$ —dotted lines), and elastic lining with higher stiffness  $K_{c_{28}} = 3400$ —solid lines). In addition, the numerical simulations include the cases with

**Fig. 30** Effect of lining stiffness on the convergence profiles for the configuration of twin tunnels with and without transverse gallery and distance between twin tunnels  $d_1 = 16R_t$ , —elastoplastic rock mass, without and with elastic lining

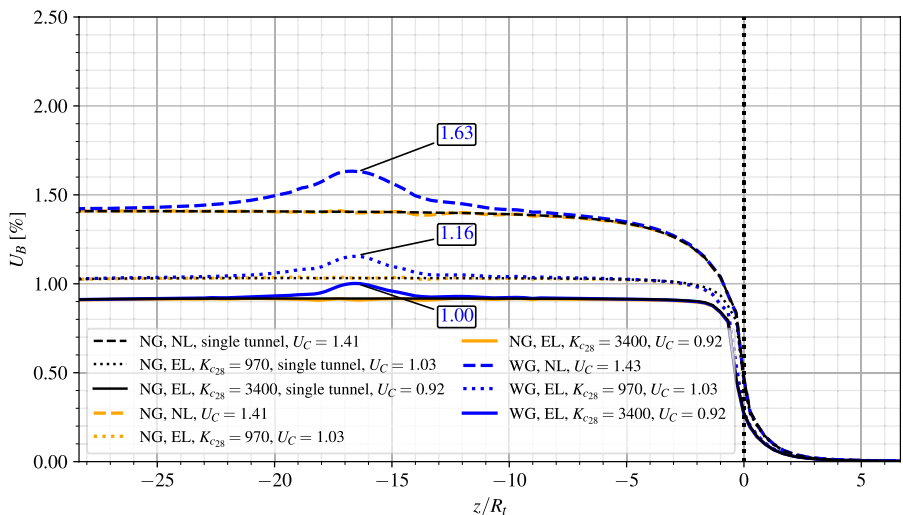
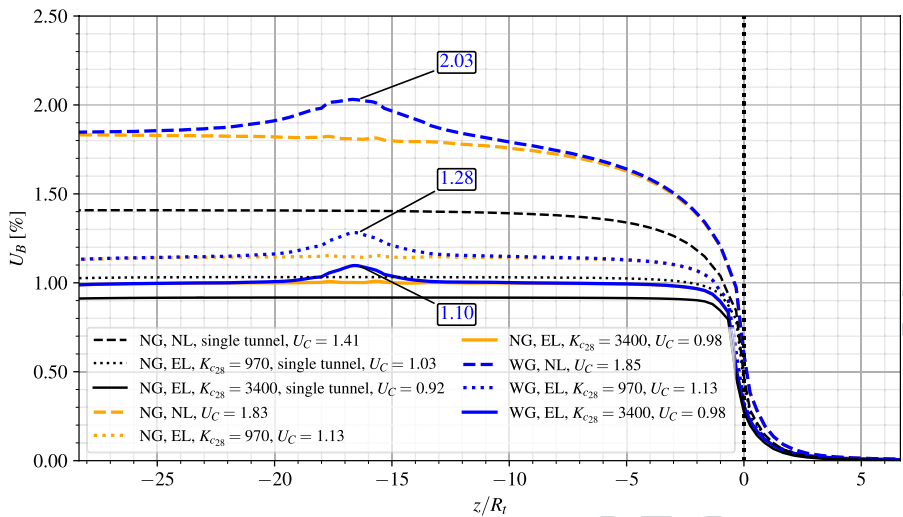


**Fig. 31** Effect of lining stiffness on the convergence profiles for the configuration of twin tunnels with and without transverse gallery and distance between twin tunnels  $d_1 = 4R_t$ , —elastoplastic rock mass, without and with elastic lining



transverse gallery (WG—blue lines) and without gallery (NG—yellow lines). The reference configuration of a single tunnel is also studied (black lines).

As observed in the simulations of preceding sections, the equilibrium convergence  $U_C$  far behind the tunnel face is almost unaffected by the presence of transverse gallery.

Regarding first the effect of lining stiffness on the convergence of single tunnel, the stiffer lining (black solid line) leads to a stabilized convergence reduction of approximately 35% with respect to unlined structure (black dashed line), whereas this reduction is only 12% for the moderate stiffness lining (black dotted line).

For twin tunnels with spacing  $d_1 = 16R_t$ , the predictions of stabilized convergence  $U_C$  (blue and yellow lines) provided in Fig. 30 are close for each lining configuration to those obtained for a single tunnel (black lines). In contrast, the interaction between the twin tunnels reveals significant when the spacing reduces to  $d_1 = 4R_t$ . In that case, the combined impact of lining support and twin tunnels proximity can be assessed by comparing in Fig. 31 the values of convergence  $U_C$  predicted for  $d_1 = 4R_t$  (yellow and blue solid lines) and  $d_1 \rightarrow \infty$  (single tunnel—black lines). Compared to the convergence of single tunnel, the increase in convergence induced by twin tunnels proximity reaches values of 30% for unlined structure, 10% for the moderate stiffness lining and 6.5% for the higher stiffness stiff.

Analyzing the effect of lining stiffness on the disturbed region associated along the convergence

profile with the presence of transverse gallery, it is first observed that the increase in stiffness reduces in all studied configurations the extent of the disturbed region, whereas the twin tunnels spacing has little impact. For the configuration of spacing  $d_1 = 16R_t$ , where the interaction due to twin tunnels proximity is expected to be minor, the ratio  $(U_{peak} - U_C)/(U_C)$  defining the relative variation between peak value and stabilized tunnel roof convergence is about 14, 12.5 and 8.7% according to the lining stiffness value:  $K_{c28} = 0$  (unlined),  $K_{c28} = 970$  MPa and  $K_{c28} = 3400$  MPa. The values of this ratio are altered to about 9.7, 13 and 12% for the configuration with spacing  $d_1 = 4R_t$ , in which both effects of lining stiffness and tunnels proximity are simultaneously acting.

In line with the previous analysis investigating the impact of instantaneous stiffness modulus  $K_{c28}$  of the lining, Figs. 32 and 33 present the long-term convergence results in the configurations of elastoplastic-viscoplastic rock mass (EPVP) and viscoelastic lining (VEL) with gallery (WG—blue lines) and without gallery (NG—yellow lines), considering twin tunnels spacing  $d_1 = 16R_t$  and  $4R_t$ , respectively. The results obtained for the reference single tunnel configuration are also provided (black lines).

Similar to the previous analysis involving constituent materials that exhibit only instantaneous behaviors, the results Fig. 32 indicate that the predictions of stabilized convergence  $U_C$  in the case of twin tunnels with spacing  $d_1 = 16R_t$  are very close to obtained for single tunnel.

**Fig. 32** Effect of instantaneous lining stiffness on the long-term convergence profiles for the configuration of twin tunnels with and without transverse gallery and distance between twin tunnels  $d_1 = 16R_t$   
—elastoplastic-viscoplastic rock mass with viscoelastic lining

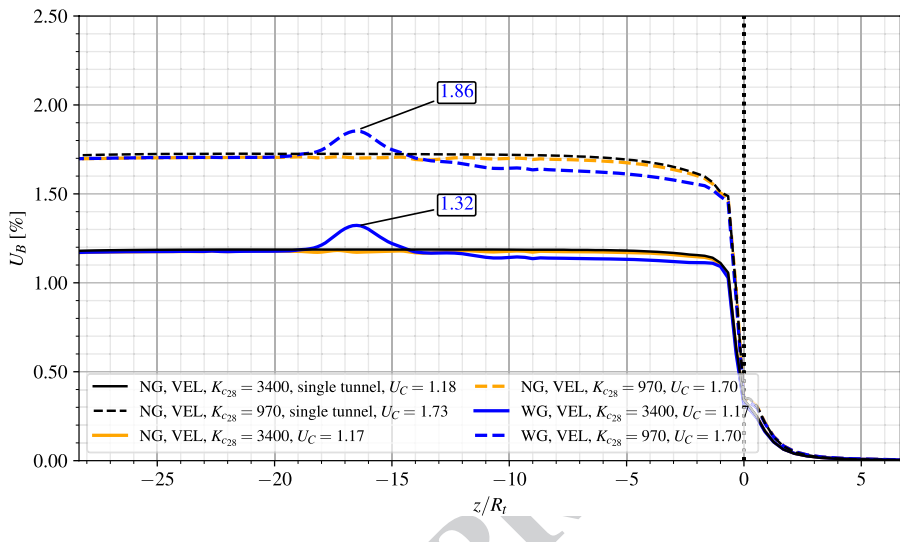


**Fig. 33** Effect of instantaneous lining stiffness on the long-term convergence profiles for the configuration of twin tunnels with and without transverse gallery and distance between twin tunnels  $d_1 = 4R_t$   
—elastoplastic-viscoplastic rock mass with viscoelastic lining

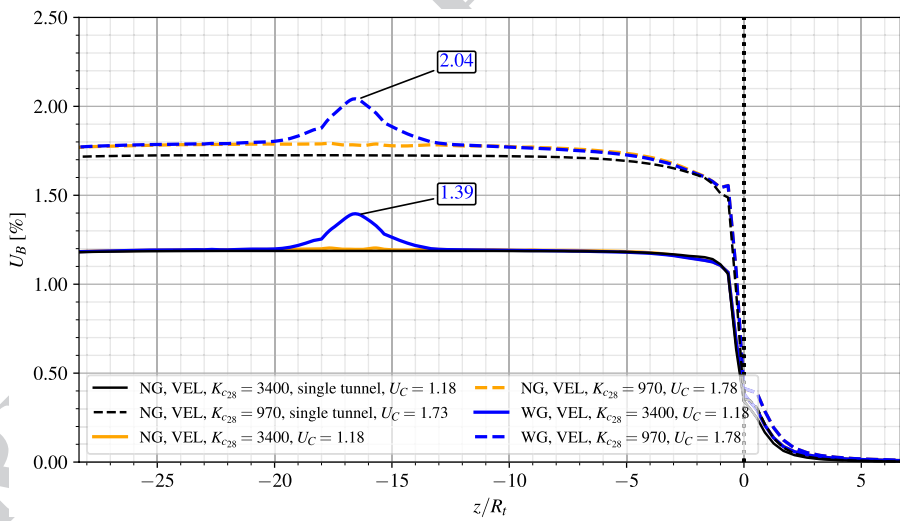


**Fig. 34** Effect of lining stiffness on the long-term convergence profiles for the configuration of twin tunnels with and without transverse gallery and distance between twin tunnels  $d_1 = 16R_t$ —elastoplastic-viscoplastic rock mass with elastic lining

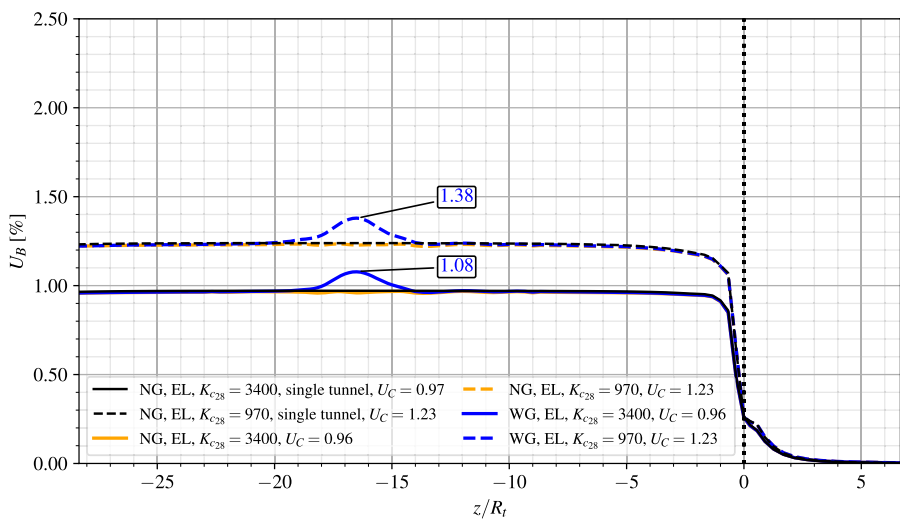
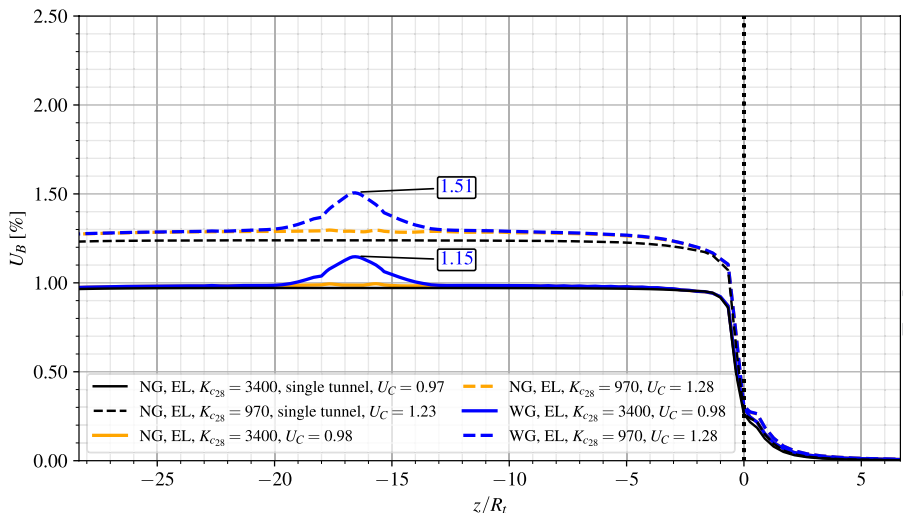


**Fig. 35** Effect of lining stiffness on the long-term convergence profiles for the configuration of twin tunnels with and without transverse gallery and distance between twin tunnels  $d_1 = 4R_t$ —elastoplastic-viscoplastic rock mass with elastic lining



Even in the specific case of  $d_1 = 4R_t$  where a strong twin tunnels interaction would be expected, the role of lining with higher stiffness on stabilized convergence (blue and yellow solid lines in Fig. 33) is predominating with values close to obtained for single tunnel (black solid line in Fig. 33), thus masking such interaction effect. For lower lining stiffness, the numerical results (blue and yellow dashed lines) indicate a small increase in the value of  $U_C$  when compared to the single tunnel (black dashed line) (Figs. 34 and 35).

As regards the impact on the peak convergence  $U_{peak}$  and extent of the gallery influence zone (disturbed portion of convergence profile), the results show that for each value of twin tunnels spacing  $d_1$ , the latter extent is slightly affected by the instantaneous lining stiffness modulus. In contrast the ratio  $(U_{peak} - U_C)/U_C$  is significantly affected by the values of  $d_1$  and  $K_{c28}$ . For the configuration with  $d_1 = 4R_t$ , it respectively takes the values  $(U_{peak} - U_C)/U_C = 14.5\%$  and  $18\%$  lower and higher lining stiffness, whereas it respectively takes the values  $9.5\%$  and  $13\%$  for the configuration with  $d_1 = 16R_t$ .

Overall, the same observations formulated in the previous analyses regarding the effect of twin tunnel spacing on stabilized convergence still hold: with respect to single tunnel configuration,  $U_C$  is almost unaffected by the lining stiffness for  $U_C$  and slightly increased (up to 4%) for  $d_1 = 4R_t$ .

With the elastic lining, the increase in stiffness from  $K_{c28} = 970$  MPa to  $K_{c28} = 3400$  MPa leads to a reduction in stabilized convergence  $U_C$  by 28% for twin tunnels spacing  $d_1 = 16R_t$  and by 16% for

$d_1 = 4R_t$ , emphasizing once again the strong mechanical interaction between the different components of the tunnel structure.

The peak value of tunnel roof convergence  $U_{peak}$  that reflects the coupling associated with intersecting transverse gallery is almost unaffected by the lining stiffness, at least for considered data parameters. In that respect, the value of ratio  $(U_{peak} - U_C)/U_C$  computed in the configuration  $d_1 = 16R_t$  (resp.  $d_1 = 4R_t$ ) is approximately 12% (resp. and 18%) for both values of lining stiffness, which corroborates the predominating effect of tunnels proximity on peak convergence  $U_{peak}$ .

## 8 Conclusions

The paper presented a constitutive and computational model for addressing the deformation processes and mechanical interactions in deep twin tunnels with connecting transverse gallery. From the constitutive viewpoint, the irreversible component of rock deformation is modeled within the context of coupled plasticity–viscoplasticity. The latter framework is particularly relevant to describe both instantaneous and delayed deformation in deep clayey rocks. Emphasis has been devoted to the formulation of aging time-dependent constitutive properties of the lining constituent material with account for shrinkage and creep deformation, which are fundamental components of early age and long-term behavior of shotcrete support. At the structure level, the computational modeling integrates the nonlinear and time-dependent

1411 constitutive features with implementation of the acti-  
 1412 vation-deactivation technique for simulating the pro-  
 1413 cesses of excavation and lining installation. The elab-  
 1414 orated model is specifically devised for dealing with  
 1415 three-dimensional finite element analysis of deforma-  
 1416 tion in twin tunnels/transverse gallery system, notably  
 1417 in the perspective of providing technical guidance for  
 1418 safe design of tunnel-gallery junction.

1419 Conceived to provide preliminary insight into  
 1420 the impact of some relevant parameters defining the  
 1421 interaction problem, the numerical simulations under-  
 1422 taken in Sect. 7 notably emphasized that:

- 1423 • The deformation anisotropy of the tunnel wall  
 1424 induced by twin tunnel proximity can be signifi-  
 1425 cant at both short-term and long-term deforma-  
 1426 tion even when a stiff lining is used. This feature  
 1427 should therefore be integrated in the support  
 1428 design stage.
- 1429 • The disturbed region with localized extent near  
 1430 the tunnel-gallery junction, reflecting the strong  
 1431 interaction between these two components of the  
 1432 structure, exhibits peak convergence values that  
 1433 can exceed by a large amount that the conver-  
 1434 gence far behind the facing. In that respect, the  
 1435 study presents the potential to formulated tech-  
 1436 nical guidance for the design of twin tunnels with  
 1437 transverse gallery.
- 1438 • In addition to the effects of coupled plastic-visco-  
 1439 plastic constitutive properties of the rock material,  
 1440 the aging time-dependent behavior considered  
 1441 for the lining concrete/shotcrete has a consider-  
 1442 able impact on the short-term and long-term con-  
 1443 vergence profiles of the tunnel. In particular, the  
 1444 aging viscoelastic lining reveals more efficient in  
 1445 controlling the long-term tunnel convergence than  
 1446 that at short term, which is mainly attributed to the  
 1447 early age properties of constituent material.

1448 Even though the numerical simulations have  
 1449 mainly concerned the situation of deep circular tun-  
 1450 nels, the constitutive and related computational model  
 1451 can in its current version be readily applied to analyze  
 1452 more complex configuration exhibiting no particular  
 1453 symmetries as that examined in this paper. In that  
 1454 respect, the following developments may be foreseen  
 1455 in the immediate future:

- The simulation of shallow depth twin tunnels con-  
 1456 nected or not by transverse galleries, commonly  
 1457 encountered in the urban underground environ-  
 1458 ment and for which the initial stress state should  
 1459 be beforehand properly evaluated. In particular,  
 1460 the modeling should address deformation and  
 1461 design of shallow twin tunnels excavated in hori-  
 1462 zontal parallel profiles or stacked over each other  
 1463 (e.g., Chakeri et al. 2011; Do et al. 2014, 2015,  
 1464 2016, 2022; Islam and Iskander 2021).  
 1465
- An important aspect to be integrated in the simu-  
 1466 lations and interaction assessment is related to  
 1467 more realistic tunneling scenario, describing the  
 1468 sequential excavation phase of each component  
 1469 of the underground structure as well as that of  
 1470 the lining placement. A significant impact of the  
 1471 lagged tunnel construction procedure, and more  
 1472 specifically the lagging distance between the faces  
 1473 of twin tunnels as well as of transverse galleries,  
 1474 is notably expected due the time-depend behavior  
 1475 of constituent materials (Ng et al. 2004; Do et al.  
 1476 2016; Islam and Iskander 2021). The numerical  
 1477 modeling and analysis of such configurations is  
 1478 currently the object of ongoing research.  
 1479
- The computational model should be extended to  
 1480 the context of poromechanical coupling. As a mat-  
 1481 ter of fact, tunnel systems are increasingly driven  
 1482 in the underwater environment, which would  
 1483 require to properly address the interaction between  
 1484 the rock mass around the tunnels and water (see  
 1485 for instance Prasetyo and Gutierrez 2018; Luo  
 1486 2020; Guo et al. 2021a, b; Chen et al. 2025, to cite  
 1487 a few recent contributions).  
 1488

Finally, it should be kept in mind that effective validation of the constitutive and computational modeling remains to be achieved through comparison of the numerical predictions with available experimental and monitoring field tunneling data.

**Author Contributions** All authors contributed to the study conception and design. Material preparation, data collection and analysis were performed by Felipe Pinto da Motta Quevedo and Carlos Colombo. The first draft of the manuscript was written by Felipe Pinto da Motta Quevedo and Samir Maghous and all authors commented on previous version of the manuscript. All authors read and approved the final manuscript.

**Funding** The authors declare that no funds, grants, or other support were received during the preparation of this manuscript.

1504 **Data Availability** Some or all data, models, or code that  
 1505 support the findings of this study are available from the cor-  
 1506 responding author upon reasonable request.

1507 **Declarations**

1508 **Conflict of interests** The authors have no relevant financial or  
 1509 non-financial interests to disclose.

1510 **References**

- 1511 Abdollahi MS, Najafi M, Bafghi AY, Marji MF (2019) A 3D  
 1512 numerical model to determine suitable reinforcement  
 1513 strategies for passing TBM through a fault zone, a case  
 1514 study: Safaroud water transmission tunnel, Iran. *Tunn  
 Undergr Space Technol* 88:186–199. [https://doi.org/10.  
 1016/j.tust.2019.03.008](https://doi.org/10.1016/j.tust.2019.03.008)
- 1515 Abdollahipour A, Marji MF, Bafghi AY, Gholamnejad J  
 1516 (2016a) Time-dependent crack propagation in a poroelas-  
 1517 tic medium using a fully coupled hydromechanical dis-  
 1518 placement discontinuity method. *Int J Fract* 199:71–87.  
<https://doi.org/10.1007/s10704-016-0095-9>
- 1519 Abdollahipour A, Marji MF, Bafghi AY, Gholamnejad J  
 1520 (2016b) A complete formulation of an indirect boundary  
 1521 element method for poroelastic rocks. *Comput Geotech*  
 1522 74:15–25. <https://doi.org/10.1016/j.compgeo.2015.12.011>
- 1523 Afifipour M, Sharifzadeh M, Shahriari K, Jamshidi H (2011)  
 1524 Interaction of twin tunnels and shallow foundation at Zand  
 1525 underpass, Shiraz metro, Iran. *Tunn Undergr Space Tech-  
 1526 nol* 26(2):356–363. [https://doi.org/10.1016/j.tust.2010.11.  
 006](https://doi.org/10.1016/j.tust.2010.11.006)
- 1527 Aguiar CB, Maghous S (2023) A micromechanics-based  
 1528 approach to damage propagation criterion in viscoelastic  
 1529 fractured materials regarded as homogenized media. *Int J  
 1530 Numer Anal Meth Geomech* 47(6):936–971. [https://doi.org/10.1002/nag.3500](https://doi.<br/>
  1531 org/10.1002/nag.3500)
- 1532 ANSYS (2018) ANSYS Programmer's Reference, release 19.2.  
 1533 ANSYS, Inc., Canonsburg, Pennsylvania
- 1534 Bažant ZP, Prasannan S (1989) Solidification theory for  
 1535 concrete creep. I: formulation. *J Eng Mech* 115(8):1691–  
 1536 1703. [https://doi.org/10.1061/\(ASCE\)0733-9399\(1989\)  
 115:8\(1691\)](https://doi.org/10.1061/(ASCE)0733-9399(1989)<br/>
  1537 115:8(1691)})
- 1538 Bažant ZP, Prasannan S (1989) Solidification theory for  
 1539 concrete creep. II: verification and application. *J Eng Mech*  
 1540 115(8):1704–1725. [https://doi.org/10.1061/\(ASCE\)0733-  
 9399\(1989\)115:8\(1704\)](https://doi.org/10.1061/(ASCE)0733-<br/>
  1541 9399(1989)115:8(1704)
- 1542 Bernaud D (1991) Tunnels profonds dans les milieux visco-  
 1543 plastiques: approches expérimentale et numérique. Ecole  
 1544 Nationale des Ponts et Chaussées, Paris, France
- 1545 Bernaud D, de Buhan P, Maghous S (1995) Numerical-sim-  
 1546 ulation of the convergence of a bolt-supported tunnel  
 1547 through a homogenization method. *Int J Numer Anal  
 1548 Meth Geomech* 19(4):267–288. [https://doi.org/10.1002/nag.1610190404](https://doi.org/10.1002/<br/>
  1549 nag.1610190404)
- 1550 Bernaud D, Maghous S, de Buhan P, Couto E (2009) A numeri-  
 1551 cal approach for design of bolt-supported tunnels regarded  
 1552 as homogenized structures. *Tunn Undergr Space Technol*  
 1553 24(5):533–546. <https://doi.org/10.1016/j.tust.2009.02.002>
- 1554 Bernaud D, Rousset G (1993) L'essai de soutènement à con-  
 1555 vergence contrôlée. In: Proceedings of International sym-  
 1556 posium, geotechnical engineering of hard soils-soft rocks.  
 1557 Athens, pp 1381–1391
- 1558 CEB-FIP (1993) CEB-FIP model code 1990: Design code.  
 1559 Comité Euro International du Béton and Fédération Inter-  
 1560 nationale de la Précontrainte (CEB-FIP)
- 1561 Chakeri H, Hasanzadeh R, Hindistan MA, Ünver B (2011) Anal-  
 1562 ysis of interaction between tunnels in soft ground by 3D  
 1563 numerical modeling. *Bull Eng Geol Env* 70(3):439–448.  
<https://doi.org/10.1007/s10064-010-0333-8>
- 1564 Chen SL, Lee SC, Gui MW (2009) Effects of rock pillar width  
 1565 on the excavation behavior of parallel tunnels. *Tunn  
 Undergr Space Technol* 24(12):148–154. [https://doi.org/10.1016/j.tust.2008.05.006](https://doi.org/<br/>
  1566 10.1016/j.tust.2008.05.006)
- 1567 Chen F, Lin L, Li D (2019) Analytic solutions for twin tun-  
 1568 neling at great depth considering liner installation and  
 1569 mutual interaction between geomaterial and liners. *Appl  
 1570 Math Model* 73:412–441. [https://doi.org/10.1016/j.apm.2019.04.026](https://doi.org/10.1016/j.apm.<br/>
  1571 2019.04.026)
- 1572 Chen J, Zeng B, Xu W, Hu S, Wang S, Wang K, Zhang W,  
 1573 Wu S, Song Z (2025) Mechanical behaviour and dam-  
 1574 age constitutive model of semi-circular arch tunnels with  
 1575 straight walls under soaking conditions. *Eng Fail Anal*  
 1576 169:109137. [https://doi.org/10.1016/j.engfailanal.2024.109137](https://doi.org/10.1016/j.engfailanal.2024.<br/>
  1577 109137)
- 1578 Chortis F, Kavvadas M (2023a) 3D numerical investigation of  
 1579 the axial forces acting on tunnel junctions constructed in  
 1580 fractured/weathered to very blocky rockmass. In: Expanding  
 1581 underground-knowledge and passion to make a positive  
 1582 impact on the world. CRC Press, pp 1574–1582
- 1583 Chortis F, Kavvadas M (2023b) 3D numerical investigation  
 1584 of the bending moments acting on tunnel junctions con-  
 1585 structed in fractured/weathered to very blocky rockmass.  
 1586 In: Expanding underground-knowledge and passion  
 1587 to make a positive impact on the world. CRC Press, pp  
 1588 1583–1591
- 1589 Chortis F, Kavvadas M (2021a) Three-dimensional numeri-  
 1590 cal investigation of the interaction between twin tunnels.  
 1591 *Geotech Geol Eng* 39:5559–5585. [https://doi.org/10.1007/s10706-021-01845-5](https://doi.org/10.1007/<br/>
  1592 s10706-021-01845-5)
- 1593 Chortis F, Kavvadas M (2021b) Three-dimensional numeri-  
 1594 cal analyses of perpendicular tunnel intersections. *Geo-  
 1595 tech Geol Eng* 39:1771–1793. [https://doi.org/10.1007/s10706-020-01587-w](https://doi.org/10.1007/<br/>
  1596 s10706-020-01587-w)
- 1597 Connor Langford J, Vlachopoulos N, Diederichs MS (2016)  
 1598 Revisiting support optimization at the Driskos tunnel  
 1599 using a quantitative risk approach. *J Rock Mech Geotech  
 1600 Eng* 8(2):147–163. [https://doi.org/10.1016/j.jrmge.2015.11.003](https://doi.org/10.1016/j.jrmge.2015.<br/>
  1601 11.003)
- 1602 de Buhan P, Fréard J, Garnier D, Maghous S (2002) Failure  
 1603 properties of fractured rock masses as anisotropic homog-  
 1604 enized media. *J Eng Mech* 128(8):869–875. [https://doi.org/10.1061/\(ASCE\)0733-9399\(2002\)128:8\(869\)](https://doi.<br/>
  1605 org/10.1061/(ASCE)0733-9399(2002)128:8(869)
- 1606 Deudé V, Dormieux L, Kondo D, Maghous S (2002) Microme-  
 1607 chanical approach to nonlinear poroelasticity: application  
 1608 to cracked rocks. *J Eng Mech* 128(8):848–855. [https://doi.org/10.1061/\(ASCE\)0733-9399\(2002\)128:8\(848\)](https://doi.<br/>
  1609 org/10.1061/(ASCE)0733-9399(2002)128:8(848)
- 1610 Do N-A, Dias D, Oreste P, Djerman-Maigne I (2014) Three-  
 1611 dimensional numerical simulation of a mechanized twin  
 1612
- 1613
- 1614
- 1615
- 1616
- 1617

- 1618 tunnels in soft ground. *Tunn Undergr Space Technol* 1619 42:40–51. <https://doi.org/10.1016/j.tust.2014.02.001>
- 1620 Do N-A, Dias D, Oreste P (2015) 3D numerical investigation 1621 on the interaction between mechanized twin tunnels in 1622 soft ground. *Environ Earth Sci* 73(5):2101–2113. <https://doi.org/10.1007/s12665-014-3561-6>
- 1623 Do N-A, Dias D, Oreste P (2016) 3D numerical investigation 1624 of mechanized twin tunnels in soft ground—fluence of 1625 lagging distance between two tunnel faces. *Eng Struct* 1626 109:117–125. <https://doi.org/10.1016/j.engstruct.2015.11.053>
- 1627 Do N-A, Dias D, Golpasand M-RB, Dang VK, Nait-Rabah O, 1628 Pham VV, Dang TT (2022) Numerical analyses of twin 1629 stacked mechanized tunnels in soft grounds—fluence of 1630 their position and construction procedure. *Tunn Undergr 1631 Space Technol* 130:104734. <https://doi.org/10.1016/j.tust.2022.104734>
- 1632 Elwood DEY, Martin CD (2016) Ground response of closely 1633 spaced twin tunnels constructed in heavily overconsolidated 1634 soils. *Tunn Undergr Space Technol* 51:226–237. <https://doi.org/10.1016/j.tust.2015.10.037>
- 1635 Fargnoli V, Boldini D, Amorosi A (2015) Twin tunnel excavation 1636 in coarse grained soils: observations and numerical 1637 back-predictions under free field conditions and in presence 1638 of a surface structure. *Tunn Undergr Space Technol* 1639 49:454–469. <https://doi.org/10.1016/j.tust.2015.06.003>
- 1640 Forsat M, Taghipoor M, Palassi M (2022) 3D FEM model on 1641 the parameters' influence of EPB-TBM on settlements of 1642 single and twin metro tunnels during construction. *Int J 1643 Pavement Res Technol* 15(3):525–538. <https://doi.org/10.1007/s42947-021-00034-0>
- 1644 Giraud A (1993) *Couplages thermos-hydro-mécaniques dans 1645 les poreux peu perméables: application aux argiles profondes*. Ecole Nationale des Ponts et Chaussées, Paris, 1646 France
- 1647 Giraud A, Rousset G (1996) Time-dependent behaviour of 1648 deep clays. *Eng Geol* 41(1):181–195. [https://doi.org/10.1016/0013-7952\(95\)00000-3](https://doi.org/10.1016/0013-7952(95)00000-3)
- 1649 Guo Z, Liu X, Zhu Z (2021a) An elastic solution for twin 1650 circular tunnels' stress in hydrostatic stress field. *Geotech 1651 Eng* 39:1–11. <https://doi.org/10.1007/s10706-021-01756-5>
- 1652 Guo P, Gong X, Wang Y, Lin H, Zhao Y (2021b) Minimum 1653 cover depth estimation for underwater shield tunnels. *Tunn 1654 Undergr Space Technol* 115:104027. <https://doi.org/10.1016/j.tust.2021.104027>
- 1655 Hoek E, Brown ET (1980) *Underground Excavations in Rock*. 1656 CRC Press
- 1657 Hsiao FY, Wang CL, Chern JC (2009) Numerical simulation of 1658 rock deformation for support design in tunnel intersection 1659 area. *Tunn Undergr Space Technol* 24(1):14–21. <https://doi.org/10.1016/j.tust.2008.01.003>
- 1660 Hsiao F, Chi-Wen YU, Chern J (2005) Modeling the behaviors 1661 of the tunnel intersection areas adjacent to the ventilation 1662 shafts in the Hsuehshan tunnel. In: Proceedings of 1663 the international symposium on design, construction and 1664 operation of long tunnels, Taipei, pp 81–89
- 1665 Insam R, Wahlen R, Wieland G (2019) Brenner Base Tunnel 1666 – interaction between underground structures, complex 1667 challenges and strategies. In: Peila D, Viggiani G, Celestino T (eds) *Tunnels and Underground Cities: Engineering 1668 and Innovation meet Archaeology, Architecture and Art*. 1669 CRC Press, pp 3857–3865. <https://doi.org/10.1201/9780429424441-408>
- 1670 Islam MS, Iskander M (2021) Twin tunnelling induced ground 1671 settlements: a review. *Tunn Undergr Space Technol* 1672 110:103614. <https://doi.org/10.1016/j.tust.2020.103614>
- 1673 Karakus M, Ozsan A, Başarır H (2007) Finite element analysis 1674 for the twin metro tunnel constructed in Ankara Clay, 1675 Turkey. *Bull Eng Geol Env* 66(1):71–79. <https://doi.org/10.1007/s10064-006-0056-z>
- 1676 Li Y, Jin X, Lv Z, Dong J, Guo J (2016) Deformation and 1677 mechanical characteristics of tunnel lining in tunnel 1678 intersection between subway station tunnel and construction 1679 tunnel. *Tunn Undergr Space Technol* 56:22–33. <https://doi.org/10.1016/j.tust.2016.02.016>
- 1680 Ling C (1948) On the stresses in a plate containing two circular 1681 holes. *J Appl Phys* 19(1):77–82. <https://doi.org/10.1063/1.1697875>
- 1682 Liu H, Li S, Li L, Zhang Q (2017) Study on deformation 1683 behavior at intersection of adit and major tunnel in railway. *KSCE J Civ Eng* 21(6):2459–2466. <https://doi.org/10.1007/s12205-017-2128-y>
- 1684 Luo Y (2020) Influence of water on mechanical behavior of 1685 surrounding rock in hard-rock tunnels: an experimental 1686 simulation. *Eng Geol* 277:105816. <https://doi.org/10.1016/j.enggeo.2020.105816>
- 1687 Ma Y, Lu A, Zeng X, Cai H (2020) Analytical solution for 1688 determining the plastic zones around twin circular tunnels 1689 excavated at great depth. *Int J Rock Mech Min Sci* 1690 136:104475. <https://doi.org/10.1016/j.ijrmms.2020.104475>
- 1691 Maghous S, Bernaud D, Fréard J, Garnier D (2008) Elasto- 1692 plastic behavior of jointed rock masses as homogenized media 1693 and finite element analysis. *Int J Rock Mech Min Sci* 1694 45(8):1273–1286. <https://doi.org/10.1016/j.tust.2012.04.008>
- 1695 Maghous S, Bernaud D, Couto E (2012) Three-dimensional 1696 numerical simulation of rock deformation in bolt-supported 1697 tunnels: a homogenization approach. *Tunn Undergr Space 1698 Technol* 31:267–288. <https://doi.org/10.1016/j.tust.2012.04.008>
- 1699 Maghous S, Dormieux L, Kondo D, Shao JF (2013) Micro- 1700 mechanics approach to poroelastic behavior of a jointed 1701 rock. *Int J Numer Anal Meth Geomech* 37:111–121. 1702 <https://doi.org/10.1002/nag.1087>
- 1703 Maghous S, Winiawer JEB, Dutra VFP (2014a) Stability 1704 analysis of tunnels driven in jointed rocks by means of a 1705 homogenized limit analysis approach. *Int J Numer Anal 1706 Meth Geomech* 38:2009–2032. <https://doi.org/10.1002/nag.2302>
- 1707 Maghous S, Lorenci G, Bittencourt E (2014b) Effective 1708 poroelastic behavior of a jointed rock. *Mech Res Commun* 1709 59:64–69. <https://doi.org/10.1016/j.mechrescom.2014.03.004>
- 1710 Marmier R, Jeannin L, Barthélémy JF (2007) Homogenized 1711 constitutive laws for rocks with elastoplastic fractures. 1712 *Int J Numer Anal Meth Geomech* 31(10):1217–1237. 1713 <https://doi.org/10.1002/nag.595>
- 1714 Nemat-Nasser S, Hori M (1993) *Micromechanics: overall 1715 properties of heterogeneous materials*. North-Holland 1716

- 1739 Ng CW, Lee KM, Tang DK (2004) Three-dimensional  
1740 numerical investigations of new Austrian tunnelling  
1741 method (NATM) twin tunnel interactions. *Can Geotech J* 41(3):523–539. <https://doi.org/10.1139/T04-008> 1792
- 1742 Nguyen Minh D, Rousset G (1987) influence of instantaneous  
1743 failure on time dependent behavior of underground galleries. In: The 28th U.S. symposium on rock mechanics (USRMS). Tucson, Arizona, pp ARMA-87-0663(06) 1793
- 1744 Nikadat N, Marji MF (2016) Analysis of stress distribution  
1745 around tunnels by hybridized FSM and DDM considering the influences of joints parameters. *Geomech Eng*  
1746 11(2):269–288. <https://doi.org/10.12989/gae.2016.11.2.269> 1794
- 1747 Nyren R (1998) Field measurements above twin tunnels in  
1748 London Clay. Imperial College London, UK, England 1795
- 1749 Panet, M (1995) Le Calcul des Tunnels par la Méthode Convergence-Confinement. Presses De L'Ecole Nationale Des  
1750 Ponts Et Chaussees 1796
- 1751 Pedro AMG, Grazina JCD, Sousae JNVA (2022) Lining forces in tunnel interaction problems. *Soils and Rocks*  
1752 45(3):22077221. <https://doi.org/10.28927/SR.2022.077221> 1797
- 1753 Perzyna P (1966) Fundamental problems in Viscoplasticity. In:  
1754 Advances in Applied Mechanics. pp 243–377 1798
- 1755 Fortsakis Petros, Bekri E, Prountzopoulos G, Marinos P (2012)  
1756 Numerical analysis of twin tunnels interaction. In: Proceedings 1st Eastern European Tunnelling Conference.  
1757 Budapest, Hungary, pp 1–8 1799
- 1758 Phutthananon C, Lertkultanon S, Jongpradist P, Duangsano O,  
1759 Likitlersuang S, Jamsawang P (2023) Numerical investigation on the responses of existing single piles due to  
1760 adjacent twin tunneling considering the lagging distance. *Underground Space* 11:171–188. <https://doi.org/10.1016/j.undsp.2022.12.005> 1800
- 1761 Piepi GT (1995) Comportement viscoplastique avec rupture  
1762 des argiles raides. Applications aux ouvrages souterrains. PhD Thesis (in French), Ecole Nationale des Ponts et  
1763 Chaussées, Paris, France. <https://theses.hal.science/tel-00523616/fr/> 1801
- 1764 Pöttler R (1992) Three-dimensional modelling of junctions  
1765 at the channel tunnel project. *Num Anal Meth Geomech*  
1766 16(9):683–695. <https://doi.org/10.1002/nag.1610160906> 1802
- 1767 Prasetyo SH, Gutierrez M (2018) Effect of transient coupled  
1768 hydro-mechanical response on the longitudinal displacement  
1769 profile of deep tunnels in saturated ground. *Tunn Undergr Space Technol* 75:11–20. <https://doi.org/10.1016/j.tust.2018.02.003> 1803
- 1770 Quevedo FPM (2017) Comportamento a longo prazo de túneis  
1771 profundos revestidos com concreto: modelo em elementos  
1772 finitos. Federal University of Rio Grande do Sul, Porto  
1773 Alegre, Brazil 1804
- 1774 Quevedo FPM (2021) Análise computacional das deformações em túneis profundos considerando o acoplamento  
1775 plasticidade-viscoplasticidade. Federal University of Rio  
1776 Grande do Sul, Porto Alegre, Brazil 1805
- 1777 Quevedo FPM, Schmitz RJ, Morsch IB et al (2018) Customization of a software of finite elements to analysis of concrete  
1778 structures: long-term effects. *IBRACON Struct Mater J* 11(4):696–718. <https://doi.org/10.1590/S1983-41952018000400005> 1806
- 1779 Quevedo FPM, Bernaud D, Campos Filho A (2022) Numerical analysis of deep tunnels in viscoplastic rock mass considering the creep and shrinkage of the concrete lining. *Int J Geomech* 22(4):04022005. [https://doi.org/10.1061/\(ASCE\)GM.1943-5622.0002282](https://doi.org/10.1061/(ASCE)GM.1943-5622.0002282) 1807
- 1780 Quevedo FPM, Bernaud D, Maghous S (2022b) Numerical integration scheme for coupled elastoplastic-viscoplastic constitutive law for tunnels. *Int J Geomech* 22(10):04022181. [https://doi.org/10.1061/\(ASCE\)GM.1943-5622.0002512](https://doi.org/10.1061/(ASCE)GM.1943-5622.0002512) 1808
- 1781 Rousset G (1988) Comportement mécanique des argiles profondes: Application au stockage de déchets radioactifs. Ecole Nationale des Ponts et Chaussées, Paris, France 1809
- 1782 Shaofeng L, Jincai F, Pinghua Z, Xiang L (2018) Stability analysis of two parallel closely spaced tunnels based on convergence-confinement principle. *J Constr Eng Manag* 144(6):04018041. [https://doi.org/10.1061/\(ASCE\)CO.1943-7862.0001496](https://doi.org/10.1061/(ASCE)CO.1943-7862.0001496) 1810
- 1783 Simo JC, Hughes TJR (1998) Computational Inelasticity. Springer, New York 1811
- 1784 Sjöberg J, Perman F, Leander M, Saiang D (2006) Three-dimensional analysis of tunnel intersections for a train tunnel under Stockholm. In: Proceedings of the North American tunneling 2006 conference, pp 10–15 1812
- 1785 Spyridis P, Bergmeister K (2015) Analysis of lateral openings in tunnel linings. *Tunn Undergr Space Technol* 50:376–395. <https://doi.org/10.1016/j.tust.2015.08.005> 1813
- 1786 Vlachopoulos N, Diederichs MS (2014) Appropriate uses and practical limitations of 2D numerical analysis of tunnels and tunnel support response. *Geotech Geol Eng* 32(2):469–488. <https://doi.org/10.1007/s10706-014-9727-x> 1814
- 1787 Vlachopoulos N, Vazaios I, Madjdabadi BM (2018) Investigation into the influence of excavation of twin-bored tunnels within weak rock masses adjacent to slopes. *Can Geotech J* 55(11):1533–1551. <https://doi.org/10.1139/cgj-2017-0392> 1815
- 1788 Wan MSP, Standing JR, Potts DM, Burland JB (2017) Measured short-term ground surface response to EPBM tunnelling in London Clay. *Géotechnique* 67(5):420–445. <https://doi.org/10.1680/geot.16.P.099> 1816
- 1789 Zheng G, Zhang T, Diao Y (2015) Mechanism and countermeasures of preceding tunnel distortion induced by succeeding EPBS tunnelling in close proximity. *Comput Geotech* 66:53–65. <https://doi.org/10.1016/j.comgeo.2015.01.008> 1817
- 1790 Zienkiewicz OC, Cormeau IC (1974) Visco-plasticity-plasticity and creep in elastic solids-a unified numerical solution 1818
- 1791

1847 approach. Int J Numer Meth Eng 8(4):821–845. <https://doi.org/10.1002/nme.1620080411>

1849 **Publisher's Note** Springer Nature remains neutral with regard  
1850 to jurisdictional claims in published maps and institutional  
1851 affiliations.

Springer Nature or its licensor (e.g. a society or other partner) 1852  
holds exclusive rights to this article under a publishing 1853  
agreement with the author(s) or other rightsholder(s); author 1854  
self-archiving of the accepted manuscript version of this article 1855  
is solely governed by the terms of such publishing agreement 1856  
and applicable law. 1857

UNCORRECTED PROOF

Journal:	<b>10706</b>
Article:	<b>3108</b>

## Author Query Form

**Please ensure you fill out your response to the queries raised below and return this form along with your corrections**

Dear Author

During the process of typesetting your article, the following queries have arisen. Please check your typeset proof carefully against the queries listed below and mark the necessary changes either directly on the proof/online grid or in the 'Author's response' area provided below

Query	Details Required	Author's Response
AQ1	Please confirm if the author names are presented accurately and in the correct sequence (given name, middle name/initial, family name). Author 1 Given name: [Felipe Pinto] Particle [da] Last name [Motta Quevedo] Author 2 Given name: [Carlos Alberto Magnus Maciel] Last name [Colombo]. Also, kindly confirm the details in the metadata are correct.	
AQ2	Reference (Fortsakis et al. 2012) was mentioned in the manuscript; however, this was not included in the reference list. As a rule, all mentioned references should be present in the reference list. Please provide the reference details to be inserted in the reference list.	
AQ3	Figures 34 and 35 was received; however, no citation was provided in the manuscript. Please check and confirm the inserted citation of Fig/Table is correct. If not, please suggest an alternative citation. Please note that figures should be cited in ascending numerical order in the text. and should be inside the main body of the text.	
AQ4	Reference Petros et al. (2012) is given in list but not cited in text. Please cite in text or delete from list.	